



저작자표시-비영리-변경금지 2.0 대한민국

이용자는 아래의 조건을 따르는 경우에 한하여 자유롭게

- 이 저작물을 복제, 배포, 전송, 전시, 공연 및 방송할 수 있습니다.

다음과 같은 조건을 따라야 합니다:



저작자표시. 귀하는 원저작자를 표시하여야 합니다.



비영리. 귀하는 이 저작물을 영리 목적으로 이용할 수 없습니다.



변경금지. 귀하는 이 저작물을 개작, 변형 또는 가공할 수 없습니다.

- 귀하는, 이 저작물의 재이용이나 배포의 경우, 이 저작물에 적용된 이용허락조건을 명확하게 나타내어야 합니다.
- 저작권자로부터 별도의 허가를 받으면 이러한 조건들은 적용되지 않습니다.

저작권법에 따른 이용자의 권리는 위의 내용에 의하여 영향을 받지 않습니다.

이것은 [이용허락규약\(Legal Code\)](#)을 이해하기 쉽게 요약한 것입니다.

[Disclaimer](#)

Master's Thesis

**Multi-Layered Flexible Pressure Sensors with  
Tunable Sensitivity and Linearity**

Jinyoung Myoung

Department of Chemical Engineering

Graduate School of UNIST

2019

# Multi-Layered Flexible Pressure Sensors with Tunable Sensitivity and Linearity

Jinyoung Myoung

Department of Chemical Engineering

Graduate School of UNIST

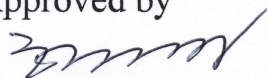
# Multi-Layered Flexible Pressure Sensors with Tunable Sensitivity and Linearity

Multi-Layered Flexible Pressure Sensors  
with Tunable Sensitivity and Linearity  
submitted to the Graduate School of UNIST  
in partial fulfillment of the  
requirements for the degree of

Jinyoung Myoung

07. 09. 2019.

Approved by



---

Advisor

Hyunhyub Ko

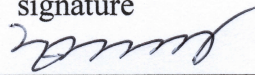
# Multi-Layered Flexible Pressure Sensors with Tunable Sensitivity and Linearity

Jinyoung Myoung

This certifies that the thesis/dissertation of Jinyoung Myoung is approved.

07.09.2019 of submission

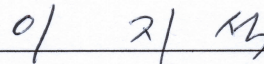
signature



---

Advisor: Hyunhyub Ko

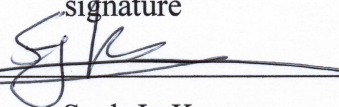
signature



---

Jiseok Lee

signature



---

Seok Ju Kang

## Abstract

Tunable sensitivity and linearity of flexible pressure sensors are the critical requirements for various user-friendly customized application such as wearable devices, prosthesis and smart robotics. However, flexible pressure sensors with both high sensitivity and linearity over broad pressure range have been rarely demonstrated. Here, we demonstrate a highly-sensitive and linearly-responsive flexible pressure sensor, which is achieved by multi-layering of PEDOT:PSS/PUD composites with interlocked structures. The multi-layer with different conductivity enables easy regulation of the change of composite resistance in response to the applied pressure. Multi-layered pressure sensors could linearly perceive the pressure over broad working pressure range of 100 kPa with the sensitivity of  $3.1 \times 10^5 \text{ kPa}^{-1}$ , which is the highest one among the pressure sensors reported so far. In addition, it shows a rapid response time of 130 ms and relaxation time of 13 ms and high durability over 5000 repetitive cycles under the pressure of 20 kPa. Owing to the high sensitivity, it can discriminate weak gas flow with different air density, delicate hand manipulation of objects and different pulse rate of carotid artery and internal jugular vein.



## Contents

### I . Introduction

1.1 Pressure sensors in electronic skins -----	1
1.2 Piezoresistive pressure sensors -----	3
1.3 Bio-inspired structures in piezoresistive pressure sensors -----	5
1.4 Materials for pressure sensor -----	7
1.5 Application of pressure sensor -----	9
1.6 Research goal -----	11

### II . Experiments

2.1 Conductivity control of PEDOT:PSS -----	26
2.2 Fabrication of substrates with interlocked structures -----	27
2.3 Characterization -----	28

### III. Results and Discussion

3.1 Sensing performance of multi-layered sensor -----	32
---	----



3.2 Effect of conductivity and thickness of layers -----	34
3.3 Comparison of sensitivity -----	36
3.4 Structural contribution to multi-layered sensors -----	37
3.4 Durability and reliability of the multi-layered sensors -----	39
3.5 Applications of pressure sensors -----	40
IV. Conclusion -----	53
V. References -----	54

## List of figures

**Figure 1.1.** The schematic illustration of the remote healthcare monitoring in human-machine interfaces and big data. (a) The requirements for e-skins, which is flexibility, stretchability, self-healing, biocompatibility and biodegradability. (*Advanced Science* **2019**, 1900186.) (b) Detection of bio-signal by e-skins attached on the wrist. (c) Wireless transportation of detected data to mobile utilities. (d) Diagnosis by professionals. (e) Uploading to cloud for accumulation of medical data. (f) Data analysis.

**Figure 1.2.** Healthcare monitoring by skin-attachable e-skins with various expression method. (a) Organic optical e-skins in which the voltage differs by applied strain on the body. (*Science advances* **2016**, 2, e1501856.) (b) Schemes of pressure sensor and skin-attachable OLED. *ACS nano* **2017**, 11, 10032.) (c) Detection of blood pressure on the forehead. (*Nature communications* **2014**, 5, 4779.) (d) Pressure sensor for the detection of subtle vibration of the neck and diagnosis of dysphagic. (*ACS nano* **2018**, 12, 5913.)

**Figure 1.3.** Detection of vital signal of the human body using flexible and skin-mountable pressure sensor and application in healthcare monitoring (a) Photograph showing wrist attached with pressure sensor and detected pulse rate, which includes the characteristic peaks of P1, P2 and P3. (b) Photograph of pressure sensor attached on the nostril and detection of respiration and discrimination of weak breath and deep breath. (Lee et al. *ACS nano* **2018**, 12, 4045.) (c) Monitoring motion of the human body including elbow motion when grasping and open, leg motion when stretches and bends, and vibration of the throat when saying. (Zhao et al. *ACS nano* **2017**, 11, 8590.) (d) Various diseases and syndromes that can be detected by pressure sensor.

**Figure 1.4.** Schematic illustrations of four common transduction methods of electronic skin (a) Piezoelectricity generated by the applied pressure (b) Capacitance change by a change of dielectric constant (c) Piezoresistive type sensor, whose current increases as the intertube distance becomes closer. (Wang et al. *Adv. Sci.* **2015**, 2, 1500169) (d) Triboelectricity. (left) Triboelectric series from positive to negative trends (b) Schematic of the operating mechanism for pressure-sensing ability based on the triboelectricity in a short-circuit system. (Park et al. *J. Mater. Chem. B* **2016**, 4, 2999.)

**Figure 1.5.** Typical fabrication method for piezoresistive sensor. (a) Composite; Scheme of the composite type sensor and application of pressure, which reduces the intertube distance of conductive filler, Pressure sensor with Sea-urchin-shaped nanoparticle imbedded in PU polymer matrix. (Lee et al. *Advanced Materials* **2016**, *28*, 9364.), Hollow microstructure in composite piezoresistive sensor. (Pan et al. *Nature communications* **2014**, *5*, 3002) (b) Coating; Scheme of pressure sensor with microstructure coated with conductive material and application of pressure, Pressure sensor with micropyramid structure coated with PEDOT:PSS (Choong et al. *Advanced materials* **2014**, *26*, 3451.), Micropyramid with Ppy integrated on the co-planar electrode. (Li et al. *ACS applied materials & interfaces* **2018**, *10*, 20826.)

**Figure 1.6.** Piezoresistive e-skins with bio-inspired micro/nanostructures. (a) Schematics for electronic skins with interlocked microdome arrays. The bottom-left plot shows the wide working and the bottom-right plots show the resistance change at different mechanical stimuli (b) schematics of slit organ of spiders and crack-based highly sensitive strain sensors. The images on the right are SEM images of crack junctions for different applied strains of 0% (top) and 1% (bottom). (c) Image of the whiskers of a mammal and multifunctional artificial electronic whisker arrays. The figures on the right show three-dimensional strain (top) and temperature (bottom) distributions mapped using electronic whisker arrays. (Park et al. *J. Mater. Chem. B* **2016**, *4*, 2999.)

**Figure 1.7.** E-skins employing various microstructure (a) PVDF/rGO micro-dome interlocked structure with sensing capabilities in both piezoresistive and piezoelectric modes. (Park et al. *Science advances*, **2015**, *1*, e1500661.) (b) Porous triboelectric sensor with P(VDF-TrFE) as the upper active layer and PDMS as bottom active layer. (Ha et al. *ACS nano*, **2018**, *12*, 3964-3974.) (c) CNT/PDMS interlocked pressure sensor with micro-dome, micro-pyramid and micro-pillar. (Park et al. *NPG Asia Materials*, **2018**, *10*, 163) (d) hierarchical structure with ZnO nanowire on the micro-pillar structure. (Ha et al. *Advanced Functional Materials*, **2015**, *25*, 3203-3209.) (e) Au deposited micro-pillar structure facing with polyaniline/PET film. (Park et al. *ACS nano*, **2015**, *9*, 9974-9985.) (f) Mesoporous PVDF-film-based piezoelectric nanogenerators. (Mao et al. *Advanced Energy Materials*, **2014**, *4*, 1301624.)

**Figure 1.8.** The structural effect of micro-structure in terms of electrical tunneling effect and local stress concentration. (a) The different sensing profile of planar, single micro-dome and interlocked micro-

dome. (Park et al. *ACS nano*, **2014**. 8. 4689-4697.) (b) Scheme of the electrical tunneling effect when the surface of micro-dome contacts (c) Fine element analysis of the interlocked micro-dome structure as the applied pressure. (Park et al. *NPG Asia Materials*, **2018**. 10. 163)

**Figure 1.9.** Comparison of structural effect in interlocked micro-structure (a) The scheme of fabricated micro-structure including micro-dome, micro-pyramid and micro-pillar. (b) Fine element analysis of interlocked micro-dome, micro-pyramid and micro-pillar when pressure is applied. (c) different electrical performance of micro-dome, micro-pyramid and micro-pillar in terms of change of the current and the contact area. (Park et al. *NPG Asia Materials*, **2018**. 10. 163)

**Figure 1.10.** The endeavor to overcome the limitation of conventional pressure sensor. (a) Scheme showing the 2 different pressure sensing trends conventional pressure sensor and advanced pressure sensor. (Lee et al. *ACS nano*, **2018**. 12. 4045-4054.) (b) graphene coated hierarchical structure fabricated by chemical vapor deposition (CVD) method. (Bae et al. *Advanced Materials*, **2016**. 28. 5300-5306.) (c) Graphene hollow structure of Ni foam and encapsulation by PDMS. (Luo et al. *Advanced Materials*, **2017**. 29. 1702675.) (d) Porous structure of MWCNTs and PDMS using reverse micelles.<sup>1</sup>(Jung et al. *Advanced Materials*, **2014**. 26. 4825-4830.) (e) Multilayered structure of PVDF/rGO interlocked sensor. (Lee et al. *ACS nano*, **2018**. 12. 4045-4054.)

**Figure 1.11.** The conductive nanomaterials widely used in the fabrication of e-skins. In clockwise, carbon nanomaterials including graphene, CNTs and conductive polymers including PEDOT:PSS, polyaniline (PANI), polypyrrole (PPy) and P3HT are demonstrated. Lastly, metals including gold nanoparticles (AuNPs), silver nanowires (AgNWs), ZnO nanowires are illustrated.

**Figure 1.12.** The application field of stretchable and conductive PEDOT in energy, electronics, and biology: thermoelectrics, supercapacitors, fuel cells, solar cells, strain sensors and actuators, electrochromic devices, electronic textiles, soft robotics, electronic skin, tissue engineering, organic electrochemical transistors (OECTs), and neural interfaces. (Kayser et al. *Advanced Materials*, **2019**. 31. 1806133.)

**Figure 1.13.** Application of electronic skin in wearable devices by detection pressure of the human

body. (a) Photograph of e-skin attached on the wrist and schematic of blood pressure when cold and warm. (Park et al. *Science advances*, **2015**. *1*. e1500661.) (b) Wearable devices attached on the wrist and can detect the physiological signal of exercising volunteer. (Gao et al. *Advanced Materials*, **2017**. *29*. 1701985.) (c) Prosthesis integrated with temperature, humidity and multiple forms of strain sensor. (Hu et al. *ACS applied materials & interfaces*, **2018**. *10*. 38493-38505.) (d) Diagnosis of dysphagia by detection of subtle vibration of the neck. (Ramírez et al. *ACS nano*, **2018**. *12*. 5913-5922.) (e) Pressure sensing device attached on the forehead and detecting cerebral oximetry.<sup>2</sup>(Kim et al. *Nature communications*, **2014**. *5*. 5747. 3)

**Figure 1.14.** The main strategy of multi-layered pressure sensor and its application (a) The strategies for enhancement of sensitivity and linearity: Multi-layering, Interlocking, Modulus gradation of up and bottom substrate and interdigitated pattern on electrode (b) Applications of the e-skin for discrimination of subtle difference of tactile and pressure sensing: pressure in hand manipulation, Discrimination of carotid artery and internal jugular vein, detection of weak gas flow and test the spatial distribution and different air density with 3x3 pixel array.

**Figure 2.1.** Recipe of the PEDOT:PSS solution and sheet resistance characterization (a) Schematic illustration of the arrangement of PEDOT and PSS grain by addition polar solvent.(Kim et al. *Advanced Materials*, **2014**. *26*, 2268–2272) (b) Recipe of the PEDOT:PSS solution for better wettability and blending

**Figure 2.2.** Fabrication procedure of multi-layering e-skins (a) Sequential coating of PLL and PEDOT:PSS/PUD solution with different conductivity (b) Scheme of the interlocked e-skins. (c) Fabrication of the electrode with Pt sputtering and AgNWs spray coating.

**Figure 2.3.** SEM image of the thickness of PEDOT:PSS/PUD film coated on the microdome patterned matrix (a) Au thin film(60nm) that was sandwiched between the PEDOT:PSS/PUD film (55nm of 3 layer) on the microdome patterned CNT/PDMS matrix to distinguish the PEDOT:PSS film. (b) Au film inserted between the PEDOT:PSS/PUD film with different conductivity to discriminate each film of the PEDOT:PSS.

**Figure 2.4.** (a) The sheet resistance of PEDOT:PSS and PEDOT:PSS/PUD thin film depending on the added ethylene glycol. (b) SEM image of Pt sputtered and AgNWs spray-coated microdome TPU with different magnification.

**Figure 3.1.** The Scheme of the multi-layered e-skins interlocked with 2 different layer. (a) Scheme for demonstration of multi-layering effect on resistance change in broad working range. (b) Scheme of the interlocked PEDOT:PSS/PUD coated PDMS and TPU (c) Illustration of step-by-step compression of multi-layered PEDOT:PSS/PUD composite by the applied pressure.

**Figure 3.2.** The sensing performance of multi-layered pressure sensor with a thickness of 45nm of 1<sup>st</sup> layer. (a) Multi-layering condition with different conductivity in each layer (b-d) The variation of resistance and current and sensitivity depending on the number of layers. (e) The table showing initial and saturation resistance in each layered conditions.

**Figure 3.3.** Thickness effect in 1 layered sensor of PEDOT:PSS/PUD thin film. (a) Variation of resistance depending on the thickness and table to verify the tendency of initial and saturation resistance. (b) Current variation of 1 layered sensor.

**Figure 3.4.** Effect of thickness on the linearity of multi-layered e-skins (a-c) Sensing performance in resistance and current variation and sensitivity of 2 layered sensor. (d-f) Sensing performance in resistance and current variation and sensitivity of 3 layered sensor.

**Figure 3.5.** Sensing performance depending on the conductivity of the 2<sup>nd</sup> layer (a) Layering condition (b) Resistance variation with different conductivity of the 2<sup>nd</sup> layer (c) Current variation.

**Figure 3.6.** Structural contribution on the multi-layered pressure sensor. (a) Scheme of interlocked sensor with different modulus of substrate (b) Comparison of sensing performance of different sensor structure with 3 layered sensor and 45nm of 1<sup>st</sup> layer thickness (c) Different saturation resistance depending on the modulus of upper and bottom substrate.

**Figure 3.7.** SEM analysis of microdome patterned electrode. (a) Microdome TPU with Pt and AgNWs. (b) Microdome TPU with Pt (C) Microdome PDMS with Pt and AgNWs. (d) Microdome PDMS with Pt.

**Figure 3.8.** Reliability and stability test of multi-layered e-skins (a) Cyclic stability test of e-skin under repetitive pressure loading of 20 kPa at a frequency of 0.25 Hz. (b) Real-time monitoring of response and relaxation times for multi-layered e-skins under different pressures of 0.5 kPa and 10 kPa.

**Figure 3.9.** (a) Hysteresis curve when loading the pressure of 100 kPa and unloading. (b) Sensing performance with resistance and current variation with different applied voltage.

**Figure 3.10.** Application of highly sensitive e-skins into the gas pressure sensing (a) Scheme of weak gas flow on the multi-layered e-skin. (b) Real-time monitoring of resistance variation depending on the flow rate of the gas (c) Resistance change of e-skins as a function of the gas flow rate.

**Figure 3.11.** Application of multi-layered e-skins to health-care monitoring (a) Photograph showing the detection of pulse pressure of carotid artery of the volunteer's neck (b) Monitored real-time pulse signals from carotid artery and characteristic peaks of  $P_1$  (incident wave),  $P_2$  (tidal wave) and  $P_3$  (diastolic wave). (c) Photograph showing detection of pulse pressure of internal jugular vein of volunteer facing slightly turning left. (d) Monitored real-time pulse signals from internal jugular vein and characteristic peaks of A (Atrial contraction), C (Tricuspid bulging, Ventricular contraction) and V(systolic filling of atrium) and 2 descents; X (Atrial relaxation) and Y (Early ventricular filling).

**Figure 3.12.** Application of e-skins into holding cups with different amount of water. (a) Schematic and photograph showing the gloves attached with multi-layered sensor on the fingertip and it is holding cup containing 150g of water. (b) Real-time detection of current variation as the amounts of water increases, which corresponds to 25 g, 50 g, 100 g, 150 g, 200 g and 250 g of water.

**Figure 3.13.** Scheme of the array and application from low pressure to high pressure. (a) Scheme of fabricated 3 x 3 array. (b-e) Scheme of the spatial distribution detection with different shapes and weights on the multi-layered 3x3 pixel array

**Figure 3.14.** The scheme illustrating different air density of Ar and N<sub>2</sub> on the multi-layered sensor and detected spatial distribution.



## List of tables

**Table 1.** Linearity table of piezoresistive pressure sensor with characteristics.

## I. Introduction

### 1.1 Pressure sensors in electronic skins

Revival of IoT (Internet of Things), 5G and communication technologies brings unprecedented connection between machine-machine (M2M) and human-machine interface (HMI), which can control the machines by human intentions and provide direct feedback from machine (**Figure 1.1**).<sup>3</sup>  
<sup>4</sup> Especially, the accumulation of enormous data with highly qualified technologies such as wearable devices and data analysis enables personalized healthcare monitoring to guide the precise treatments according to medical data of users. It shifts the focus of medical treatment from hospital-centered healthcare to patient-centered healthcare, which can prevent diseases long before the appearance of clinical signs and symptoms. For the realization of personalized healthcare system into daily life, huge amounts of information about patients should be accumulated and analyzed with electronic skins (e-skins).

E-skins, which emulates the perceptive functionalities of human skin, have advanced the wearable technologies.<sup>5</sup> Although various types of wearable sensors were developed for healthcare applications, rigid forms of conventional sensors prevent them from conformally mounting on human skin, resulting in inaccurate detection of health events and inconvenience issues.<sup>6</sup> In addition, conventional planar form of e-skins exhibit poor sensing capabilities such as low sensitivity and narrow pressure detection range.<sup>7</sup>

Therefore, e-skins with flexible, light weight and skin attachable mechanical properties are demanded to be applied to skin-mountable wearable sensors.<sup>8-13</sup> Inspired by special structures and sensing capabilities of human skin, e-skins can perceive the external stimuli by transducing them into electrical or optical signals. **Figure 1.2** demonstrates the various e-skins, which detects biosignal from human body and provide visualized feedback. Progressed from the sensory capabilities of human skin that can perceive and differentiate the magnitude and distribution of various kind of external stimuli, including mechanical stimuli, humidity, temperature and subtle texture difference, e-skins have been integrated with advanced functionalities such as chemical sensors or energy harvesting devices.<sup>2, 14-18</sup> Moreover, self-healing, biocompatibility and biodegradability are additional requirements to be operated on human skin with long-term stability.

19-21

Among them, a pressure sensing device based on various mechano-transduction mechanism is key component to realize aforementioned applications (**Figure 1.3**). For example, the skin-

attachable pressure sensing devices with wireless module bring opportunities to manage the health events and prevent the diseases by detecting the vital signals of user, including blood pressure, pulse rate and respiration rate in real-time, enabling remote and personalized healthcare monitoring of various diseases, such as Parkinson's disease, sudden infant death, and hyperlipidemia.<sup>3, 22-24</sup>

Development of e-skins with calibrated and auto-tunable sensing capabilities will make them conduct the diagnosis and provide therapeutic treatment even without the manual assistance of humans.<sup>25, 26</sup> For last decades, lots of devices have been reported to improve sensing performances of the conventional e-skins and attain above requirements simultaneously based on the various mechano-transduction mechanisms such as piezo-electricity, piezo-resistivity, capacitance and triboelectricity (**Figure 1.4**).<sup>27-30</sup> The pressure sensor with piezoelectric type can produce the electrical charge under mechanical force due to the generation of electrical dipole moments. Rapid response and high sensitivity utilize the detection of dynamic pressure as well as static pressure. The triboelectric sensors utilize the electrical charge on the surface between materials with different triboelectric polarities. Because, the triboelectricity is generated temporarily, it has a disadvantage in long-term reliability. Both piezoelectric and triboelectric pressure sensors can be applied for self-powered wearable sensors due to their power generation by external stimuli. The piezoresistive and capacitance pressure sensors are suitable for the detection of static forces applied in different directions and environmental conditions such as temperature, humidity and chemicals. Piezoresistive sensor uses the change of contact resistance of bulk resistance as pressure is applied to the sensor, which is expressed as  $(\Delta R/R_0)/\Delta P$ . The pressure sensors using piezoresistivity are widely used due to their simple fabrication, easy readout mechanism. Furthermore, Capacitance is the ability to store a charge, which is defined as the equation of  $C = \epsilon A/d$ , where  $\epsilon$  is the dielectric constant, and A and d are the area and the distance between the two electrodes. By simple governing equation, the capacitive sensor has an advantage in tailoring design of device. In addition, it has high sensitivity in static stimuli and low power consumption. Therefore, depending on the target stimuli, 4 different transduction mechanism can be utilized for effective detection.<sup>31</sup>

## 1.2 Piezoresistive sensor

For precise conversion of mechanical stimuli including dynamic/static pressure, strain, shear force into electrical signals, the pressure sensing device can be operated using various mechano-transduction mechanisms such as piezoresistivity, capacitance, piezoelectricity and triboelectricity. Especially, the piezoresistive type sensor, which perceives mechanical stimuli by transducing them into change in resistance of materials, has attracted considerable research interests due to their advantages in simple fabrication process, rapid response time, and easy readout mechanism.<sup>32</sup> Piezoresistive sensors are generally based on conductive polymer composites composed of conductive materials inducing resistance change and elastomeric polymer matrix enabling elastic deformation under applied pressure.<sup>6</sup>

Accordingly, the change of electrical signal is occurred from the contact resistance ( $R_c$ ) change between active layer and electrode layer<sup>33,34</sup> or the bulk film resistance ( $R_f$ ) change by inter-distance change of conductive fillers.<sup>35,36</sup> In terms of fabrication of the piezoresistive sensors, there are two methods to integrate the electrically conductive nanomaterials in skin-like elastomeric polymer matrix; one is mixing them to form the conductive polymer composites and the other one is coating conductive materials on polymer substrates.<sup>37</sup>

In composite type of piezoresistive sensors, when the external pressure is applied to the resistive sensors, deformation of elastic polymer composites induces the decrease of inter-distance between conductive fillers, resulting in an increase in bulk film resistance ( $R_f$ ). It has an advantage in physical and chemical stability after annealing in high temperature to polymerize polymer matrix, which retains the reproducible output signal with repetitive deformation. However, piezoresistive sensors based on conductive composites with planar structure only depends on changes in bulk film resistance for pressure sensing, limiting the range of resistance change and thus induce low sensitivity.

Introduction of microstructured surface to conductive polymer composites can be a key technology to improve sensitivities of e-skins by increasing surface area. Different with e-skins with planar structure, the pressure-sensing of the e-skins with microstructures is mainly affected by changes in contact resistance, which can be easily tuned by control of microstructures.<sup>7, 38</sup> For example, in **figure 1.5a**, hollow sphere structure of polypyrrole (PPy) exhibits the sensitivity of  $133 \text{ kPa}^{-1}$  in the narrow pressure range of 280 Pa.<sup>39</sup> In addition, a pressure sensing device composed of the sea-urchin shaped nanoparticles and polyurethane (PU) achieved the sensitivity of  $2.46 \text{ kPa}^{-1}$  in low pressure regime ( $<1 \text{ kPa}$ ).<sup>36</sup> Although these e-skins show enhanced sensory performances than planar e-skins, the sensing capability is still inhibited by the low sensitivity and narrow pressure

detection range, caused by the limited deformation of material itself and limited percolation threshold.

On the other hand, using coating materials to fabricate active layers, the device integrated with PUD/PEDOT:PSS layers on PDMS micro-pyramid structures exhibits a high sensitivity of  $10.32 \text{ kPa}^{-1}$  in the pressure range lower than 4 kPa (**Figure 1.5b**).<sup>40</sup> Recently, the pressure sensor with coplanar electrode facing with micro-pyramid patterned PPy layer showed very high sensitivity of  $1907 \text{ kPa}^{-1}$ , but is limited by the low detection range of 100 Pa.<sup>41</sup> According to the above devices, pressure sensors of coating type have disadvantages in non-linear detection or narrow linear range, despite high sensitivity. Because the resistance change is only governed by the contact resistance variation, it causes faster saturation of resistance compared to the pressure sensors with composite type. Despite the high sensitivity, most of previous pressure sensors are still suffered from the limitations in non-linearity and narrow linear detection range lower than 10 kPa.<sup>42</sup> In this aspect, it is necessary to develop complementary and novel strategies for pressure sensors with both high sensitivity and linearity, which enables potential applications in wearable healthcare monitoring devices, prosthesis, smart robotics, and HMI technology.

### 1.3 Bio-inspired structures in piezoresistive pressure sensors

In the last decades, the pressure sensing devices that mimic the characteristic structure of organs in nature has emerged as one of the promising alternatives, which endows the multi-functionality and enhanced sensing capabilities. For example, the crack of the insect's slit organ<sup>43</sup>, whiskers of mammals<sup>44</sup>, roughness of leaf's structure<sup>45</sup> and interlocked structure of dermis and epidermis of human skin<sup>46</sup> provides the new strategy in design and fabrication of the pressure sensors (**Figure 1.6**). Especially, the human skin has attracted great attention due to their ideal sensory capabilities for sensitive discrimination of various tactile stimuli.<sup>47, 48</sup> It is attributed to the unique geometry of the interlocked micro-ridge structures between the dermis with lower modulus and the epidermis with high modulus.<sup>49</sup> The interlocked microstructure effectively concentrates the stress on the tip, generating localized stress, and amplifies the tactile sensation from the applied pressure, improving the sensitivity.<sup>50, 51</sup> Furthermore, the fingerprint that present on the surface of fingertip enables to perceive the tiny differences in texture.<sup>52</sup>

The sensitivity is defined by the change in the electrical signal depending on the applied pressure, which can be expressed as  $(\Delta R/R_0)/\Delta P$  or  $(\Delta I/I_0)/\Delta P$ . Therefore, to enhance the sensitivity, the gap between the initial resistance and saturation resistance should be as large as possible. Inspired by human skin, various kinds of microstructures including micro-domes, micro-pillars, micro-pyramids and micro-pores<sup>1</sup> have been employed in the elastomeric matrix, which increases the surface area of the sensors and triggers dynamic change of contact area between microstructures (**Figure 1.7**). As illustrated in **Figure 1.8**, the interlocked micro-dome patterned CNT/PDMS composite exhibits larger variation of resistance change compared to the planar one. The large variation of contact area between interlocked microstructures induces a large change in resistance by electrical tunneling effect, which enhances the sensitivity of the sensor. On the other hand, the resistance change of planar structure is dominated only by the film resistance *via* the inter-tube distance of CNTs.<sup>17</sup>

The sensing performance of various microstructures is varied due to the different contact area change (**Figure 1.9a**). **Figure 1.9b** indicates that the micro-pyramid patterned arrays exhibit the largest value in the concentrated stress under the applied pressure, due to the sharp edge of the micro-pyramid. However, the micro-dome patterned arrays experience larger variation of contact area in overall pressure range. Because change of contact area critically affects the current change, the micro-dome patterned arrays exhibit higher sensitivity compared to other patterns (**Figure 1.10c**). In the micro-pillar patterned array, it doesn't have enough small contact spot for localized stress, which has the lowest sensitivity in current change.<sup>38</sup>

To further improve performances of conventional pressure sensing devices, various approaches have been tried by controlling the microstructure. As illustrated in **Figure 1.10a**, previously reported devices are suffered from narrow detection range with the high sensitivity or non-linearity in overall detection ranges.<sup>53</sup> To resolve this problem, the hierarchical structure is suggested, which is based on hierarchical microdome-patterned PDMS coated with a monolayer of graphene (**Figure 1.10b**). It exhibited a high linearity in the pressure range under 12 kPa with the sensitivity of 8.5 kPa<sup>-1</sup>.<sup>54</sup> Moreover, the piezoresistive sensor based on the hollow structure of graphene and PDMS composite reached the sensitivity of 15.9 kPa<sup>-1</sup> in the pressure range of 60 kPa with the linear detection capability (**Figure 1.10c**).<sup>55</sup> However, the sensitivity and detection range are limited. Most recently, Lee et al employed the stacked structure of interlocked PVDF/rGO composite with a sensitivity of 47.7 kPa<sup>-1</sup> in the pressure range of 353 kPa (**Figure 1.10e**). The accumulation of localized stress in each layer enables continuous sensing without saturation over large dynamic sensing range.<sup>53</sup> However, the sensitivity of most of previous sensors is below 50 kPa<sup>-1</sup>, which is not sufficient for the detection of subtle difference of bio-signal including different pulse pressure variation (PPV) and intracranial pressure (ICP). To enhance the limited sensitivity, effective and rational strategy in fabrication is highly demanded to increase the gap between the initial resistance and saturation resistance with the linear variation.

#### 1.4 Materials in pressure sensors

As previously mentioned, the piezoresistive pressure sensor is based on the integration of the conductive filler in or on the elastomeric matrix. To effectively concentrate the stress on conductive materials and generate electrical tunneling effect, selection of materials and control of the ratio between conductive and elastic materials is a critical issue.<sup>6</sup> Conventionally, pressure sensitive rubber (PSRs) is fabricated using patterned metal-based components integrated on field effect transistors.<sup>56</sup> With rigid and stable conductivity formation, many metal-based materials have been used in the early stages of pressure sensor development, which includes gold<sup>22</sup>, silver<sup>57</sup> or liquid metal<sup>58</sup>. However, the low sensitivity and a large hysteresis of these materials brings the need of new strategy in the fabrication of pressure sensors. Therefore, the conductive polymers have been used, satisfying the good electrical performance, a large area processability and cost effectiveness.<sup>59</sup> In addition, for compatibility with human skin, a flexible, stretchable and chemically inert substrate is necessary. In respect to mentioned requirements, the properties of widely used materials in pressure sensors are described below and in **Figure 1.11**.

**Materials for substrates** : As one of the widely used substrate for the piezo-resistive pressure sensor, polydimethylsiloxane (PDMS) has high chemical inertness, stability, transparency, mechanical properties. Furthermore, polyurethane (PU), poly(styrene-block-butadiene-styrene) (SBS) and ecoflex silicone elastomers are used as flexible polymer matrix.<sup>37</sup>

**Silver nanowires (AgNWs)** : Silver nanowire is widely used in pressure sensor and transparent electrode due to their many advantages. It possesses high transparency and mechanical/electrical properties by the large aspect ratio. In addition, the cost-effectiveness and large-scale solution-based process, including spin coating, drop casting, rod casting, and spray coating enables the application into various fields.<sup>60,61</sup>

**Carbon materials** : As a representative of conductive materials, there are carbon nanoparticles, carbon nanotubes (CNTs), carbon nanomesh, reduced graphene oxide and graphene. Especially, CNTs can be fabricated without high purification and produced in large-scale by solution deposition technique including vacuum filtration, spin-coating, spray-coating and inkjet printing. The electrical stability and outstanding mechanical properties of CNTs enable the rapid progress in enhancing the capabilities of pressure sensors.<sup>62</sup> As a second carbon allotrope, graphene and reduced graphene oxide has exceptional electrical transport properties. Graphene with the highest surface-to-volume ratio enables the wide range detection compared to CNTs. In addition, its conductivity and mechanical stability of pristine graphene can be enhanced by reduction of chemical, thermal, photothermal and electrochemical methods.<sup>63</sup> However, carbon-based materials



exhibit low transparency due to their deep color.

**Conductive polymers** : Conductive polymers include poly(3-hexylthiophene) (P3HT), polyaniline(PANI), polypyrrole (PPY), poly(3,4-ethylenedioxythiophene)poly(styrenesulfonate) (PEDOT:PSS), and their derivatives.<sup>6</sup> Chemical and physical properties of them can be easily controllable by the rearrangement of the molecular structure during the synthesis process, which can also affects to the electrical stability and performance when used in pressure sensors.<sup>64</sup>

Among them, PEDOT:PSS has been used for the sensors for the detection of pressure, strain, humidity and chemicals, energy harvesting devices including thermoelectrics, solar cells and supercapacitors and transparent electrodes (**Figure 1.12**). It is well known as a complex of conductive PEDOT and insulator PSS as doped materials.<sup>65</sup> The addition of PSS helps to increase water solubility and enables easy solution-based process such as spin-coating, inkjet printing and spray coating. However, pristine PEDOT:PSS has relatively low conductivity compared to the metal-based conductive fillers such as AgNWs, AuNPs or carbon based materials to be used for sensitive pressure sensors. The low conductivity is because the short, hydrophobic and conductive PEDOT micelles are encircled by a hydrophilic and insulator PSS shell. The low conductivity can be easily overcome by the addition of polar additives such as ethylene glycol, dimethyl sulfoxide (DMSO) and triton X or post treatment, which enhances the conductivity.<sup>66, 67</sup> These process removes the excess PSS and rearrange conductive PEDOT micelles for the better organization.<sup>68</sup> Furthermore, for the application into stretchable electronics, the brittleness of pristine PEDOT:PSS should be modified by the addition of surfactants or polyurethane dispersion (PUD) as elastomer.<sup>40</sup>

## 1.5 Application of pressure sensors

Owing to the development of 5G wireless communication and artificial intelligence including internet of things (IoT), human-machine interface is actively connected and generalized, which facilitates the easy access of wearable devices of public.<sup>69</sup> Especially, due to the interest in improvement of quality of life and convenient health care devices, lots of wearable devices for personalized health care systems have been developed in last decades.<sup>70</sup> Skin-attachable, light-weight and biocompatible properties of e-skins enables the integration on the human body with conformal contact and be able to detect the vital body parameters including pulse wave, blood pressure and motion of body in real time. Electronic skins with accurate and reliable sensing capabilities can be applied into various fields including wearable healthcare devices, prosthesis and robotics.

As one of the vital signals of the human body, abnormal pulse rate indicates the hypertension, hyperlipidemia and hardening of the arteries. Micro-dome patterned PVDF/rGO composites with interlocked structures exhibit high sensitivity, which can detect the subtle change of pressure on the surface of the human body including characteristic peaks P1, P2 and P3, which represents the incident, tidal, and diastolic waves, respectively (**Figure 1.13a**).<sup>17</sup>

Additionally, the wearable sensors can monitor the body motion and blood pressure for electrocardiogram (ECG), electroencephalography (EEG) and electromyogram (EMG) analysis. To conduct above measurements, the sensors should be intimately integrated on the human body without void because the human skin and organs are curved surfaces that move dynamically.<sup>71</sup> The conformal contact between wearable sensors and surface of human skin enables more accurate and precise sensing results of various bio-signals. In **Figure 1.13c**, the adhesion force is enhanced by employing Triton X in the PDMS elastomers. The adhesion force increases 7 times compared to pristine PDMS films, which resulted in better conformal contact with the surface of the skin and achievement of higher ECG peaks compared to commercial-gel-based ECG sensors.<sup>72</sup> Moreover, Rapid body motion can be detected by the pressure or strain signals on the wearable sensors, which enables the diagnosis of Parkinson's disease and sensitive and accurate detection of the hyperlipidemia and dysphagia (**Figure 1.13d**).<sup>73, 74</sup>

Prosthesis, which replaces the missing body part lost by unexpected incidents or congenital disorder, can be advanced by the integration of electronic skins. Realization of perceptible prosthesis and returning the function of perception provide social, economical and self-realizable opportunities for users and brings positive effect to the whole society. The nanocomposite composed of electrostatic assembly of cationic polystyrene and graphene oxide and AgNWs is

utilized for prosthetic forefinger which monitors the bending motion.<sup>10</sup> It accurately discerns the different bending angle of each fingers. By the multidimensional structures using 1, 2 and 3D materials, they achieved high electrical conductivity despite the low percolation threshold. In addition, in **figure 1.13e**, the prosthesis that can simultaneously detect temperature, humidity and multiple forms of strain is demonstrated. Exquisite array devices possess fine mechanical reliability and high sensitivity in response to the variable ambient surroundings.<sup>2</sup>

## 1.6 Research goal

The pressure sensing devices have developed to satisfy various requirements including high sensitivity, linearity, rapid response time, durability and wide detection range. Even though simultaneous achievement of all of them is largely challenged, it should be satisfied for practical applications in real life. One step further, the realization of large quantity production and easy fabrication process of sensors should be established.<sup>75</sup> To develop a sensor that satisfies all of the above conditions, rational and novel strategies in the materials choice and device fabrication are highly needed.

In this work, we demonstrate an unprecedented strategy to fabricate the pressure sensing device with the highest pressure sensitivity among the sensors reported so far (**Figure 1.14**). The device exploits interlocked structure of micro-dome patterned PDMS as the active layer and TPU as the electrode layer, which is inspired by the interlocked micro-ridge structure of human skin. The prominent feature of our design is the multi-layered conductive polymer, PEDOT:PSS, with different conductivity to control the initial and saturation resistance, which is the main factor to determine the sensitivity of the sensors. The rapid saturation of resistance in previously reported interlocked structures was complemented by the simple multi-coating of PEDOT:PSS solution with various conductivity, inducing the gradual change of resistance in a film. The tuned conductivity of 1st and 3rd layer in multilayered PEDOT:PSS generates huge resistance changes from 109  $\Omega$  to 102  $\Omega$ , which leads to the high sensitivity in the large pressure range under 100 kPa. Additionally, stable maintenance of sensitivity without saturation was achieved by means of the medium ranged the conductivity of the 2nd layer in multilayered PEDOT:PSS. Depending on the number of layers, the sensitivity of the pressure detection can be easily tuned. Moreover, the thickness and conductivity of each layer affects the linearity. Therefore, the linearity and sensitivity can be tuned by simple spin-coating of PEDOT:PSS with different conductivity.



**Figure 1.1.** The schematic illustration of the remote healthcare monitoring in human-machine interfaces and big data. (a) The requirements for e-skins, which is flexibility, stretchability, self-healing, biocompatibility and biodegradability.<sup>76</sup>(*Advanced Science* **2019**, 1900186.) (b) Detection of bio-signal by e-skins attached on the wrist. (c) Wireless transportation of detected data to mobile utilities. (d) Diagnosis by professionals. (e) Uploading to cloud for accumulation of medical data. (f) Data analysis.

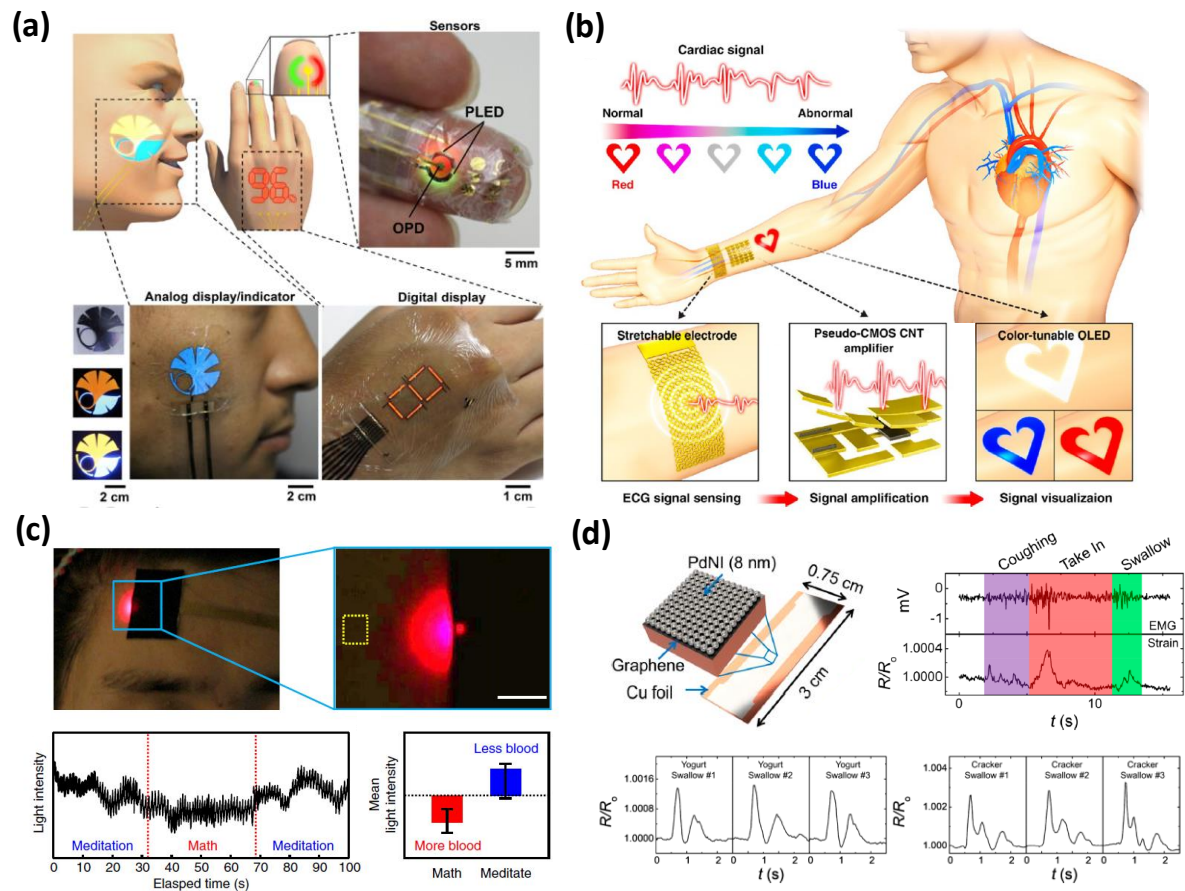


**Figure 1.2.** Healthcare monitoring by skin-attachable e-skins with various expression method. (a) Organic optical e-skins in which the voltage differs by applied strain on the body.<sup>77</sup>(*Science advances* **2016**, *2*, e1501856.) (b) Schemes of pressure sensor and skin-attachable OLED.<sup>12</sup>(*ACS nano* **2017**, *11*, 10032.) (c) Detection of blood pressure on forehead.<sup>73</sup>(*Nature communications* **2014**, *5*, 4779.) (d) Pressure sensor for the detection of subtle vibration of the neck and diagnosis of dysphagic.<sup>74</sup>(*ACS nano* **2018**, *12*, 5913.)

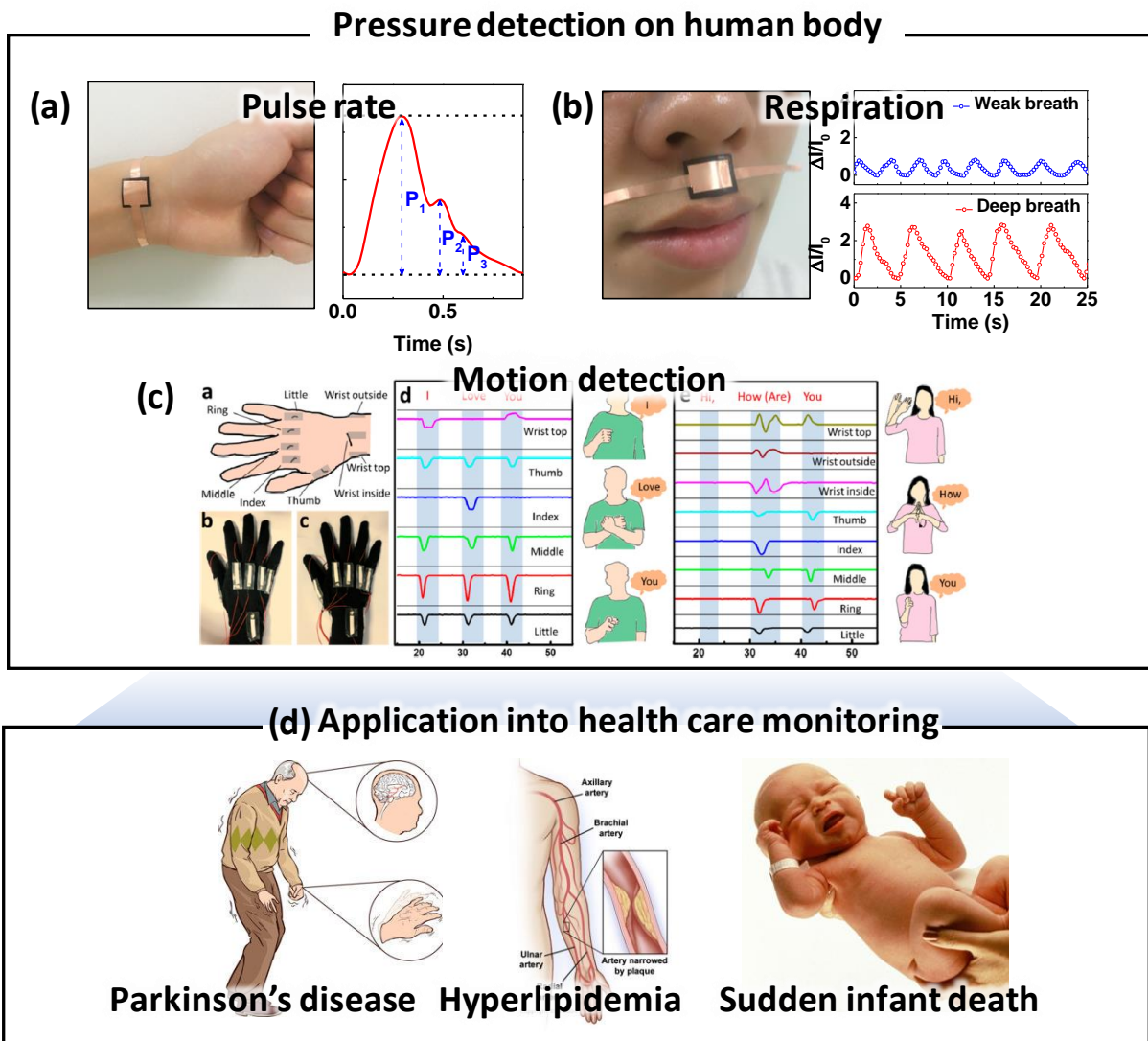


**Figure 1.3.** Detection of vital signal of human body using flexible and skin-mountable pressure sensor and application to healthcare monitoring (a) Photograph showing wrist attached with pressure sensor and detected pulse rate, which includes the characteristic peaks of P1, P2 and P3.<sup>53</sup> (b) Photograph of pressure sensor attached on the nostril and detection of respiration and discrimination of weak breath and deep breath.<sup>53</sup> (Lee et al. *ACS nano* **2018**, *12*, 4045.) (c) Monitoring motion of human body including elbow motion when grasping and open, leg motion when stretches and bends, and vibration of the throat when saying.<sup>78</sup> (Zhao et al. *ACS nano* **2017**, *11*, 8590.) (d) Various diseases and syndromes that can be detected by pressure sensor.

	Static force detection		Dynamic force detection / Energy harvesting	
	(a) piezoresistive	(b) Capacitive	(c) Piezoelectric	(d) Triboelectric
Working Mechanism				
Advantages	Simple fabrication Easy readout process Fast response time	High sensitivity Fast response time Low power consumption	High sensitivity to dynamic stimuli	Sustainable energy source
Disadvantages	Power consumption Temperature dependent	Non-linear detection Sensitive to vibration	Complicated sensor design	Long-term unreliability

**Figure 1.4.** Schematic illustrations, advantages and disadvantages of four common transduction methods of electronic skin (a) Piezoelectricity generated by the applied pressure (b) Capacitance change by a change of dielectric constant (c) Piezoresistive type sensor, whose current increases as the intertube distance becomes closer.<sup>31</sup> (Wang et al. *Adv. Sci.* **2015**, 2, 1500169) (d) Triboelectricity. Schematic of the operating mechanism for pressure-sensing ability based on the triboelectricity in a short-circuit system.<sup>5</sup> (Park et al. *J. Mater. Chem. B* **2016**, 4, 2999.)



## Fabrication of piezoresistive pressure sensor

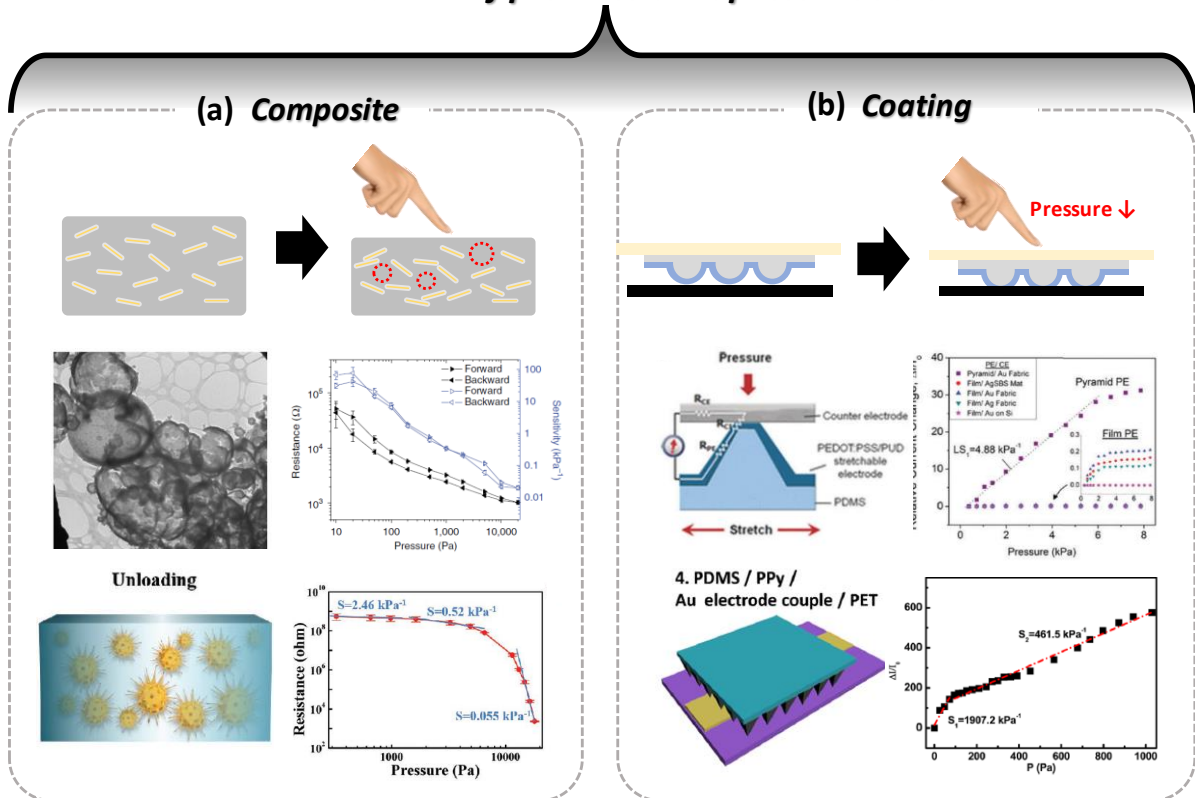


**Figure 1.5.** Typical fabrication method for piezoresistive sensor. (a) Composite; Scheme of the composite type sensor and application of pressure, which reduces the intertube distance of conductive filler, Pressure sensor with Sea-urchin shaped nanoparticle imbedded in PU polymer matrix<sup>36</sup>(Lee et al. *Advanced Materials* **2016**, *28*, 9364.), Hollow microstructure in composite piezoresistive sensor<sup>39</sup>(Pan et al. *Nature communications* **2014**, *5*, 3002) (b) Coating; Scheme of pressure sensor with microstructure coated with conductive material and application of pressure, Pressure sensor with micropyramid structure coated with PEDOT:PSS<sup>40</sup>(Choong et al. *Advanced materials* **2014**, *26*, 3451.), Micropyramid with Ppy integrated on the co-planar electrode.<sup>41</sup>(Li et al. *ACS applied materials & interfaces* **2018**, *10*, 20826.)

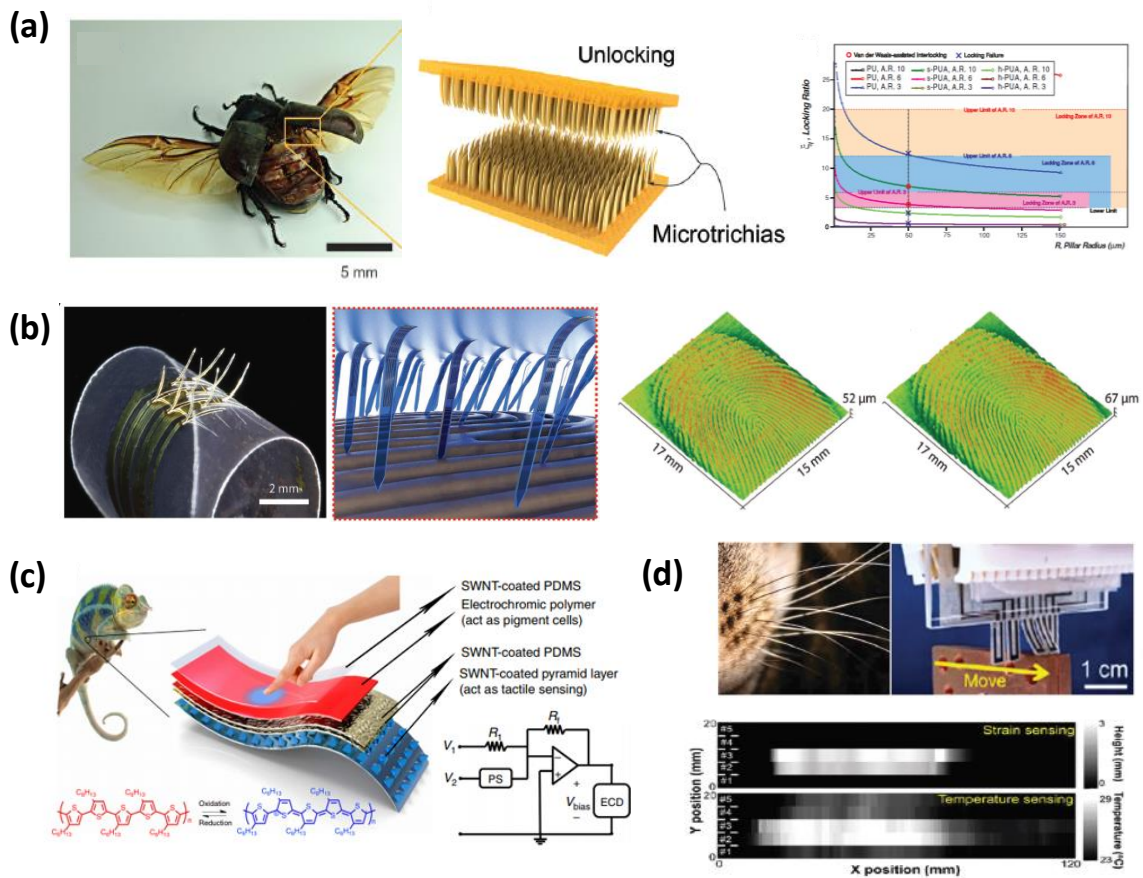


**Figure 1.6.** e-skins with bio-inspired micro/nanostructures. (a) beetle wing inspired interlocking structure for shear adhesion.<sup>79</sup>(*Adv. Mater.* **2012**, *24*, 475.) (b) Whisker inspired 3D structure for scalable detection of proximity, surface topology, friction, force.<sup>80</sup>(*Adv. Mater.* **2018**, *30*, 1706733.) (c) Chameleon inspired tactile sensing device with providing real-time color change.<sup>81</sup>(*Nature communications* **2015**, *6*, 8011.) (d) mammal's whisker inspired e-skin, which can detect the thermal and mechanical stimuli simultaneously.<sup>82</sup>(*ACS nano* **2014**, *8*, 3921.)

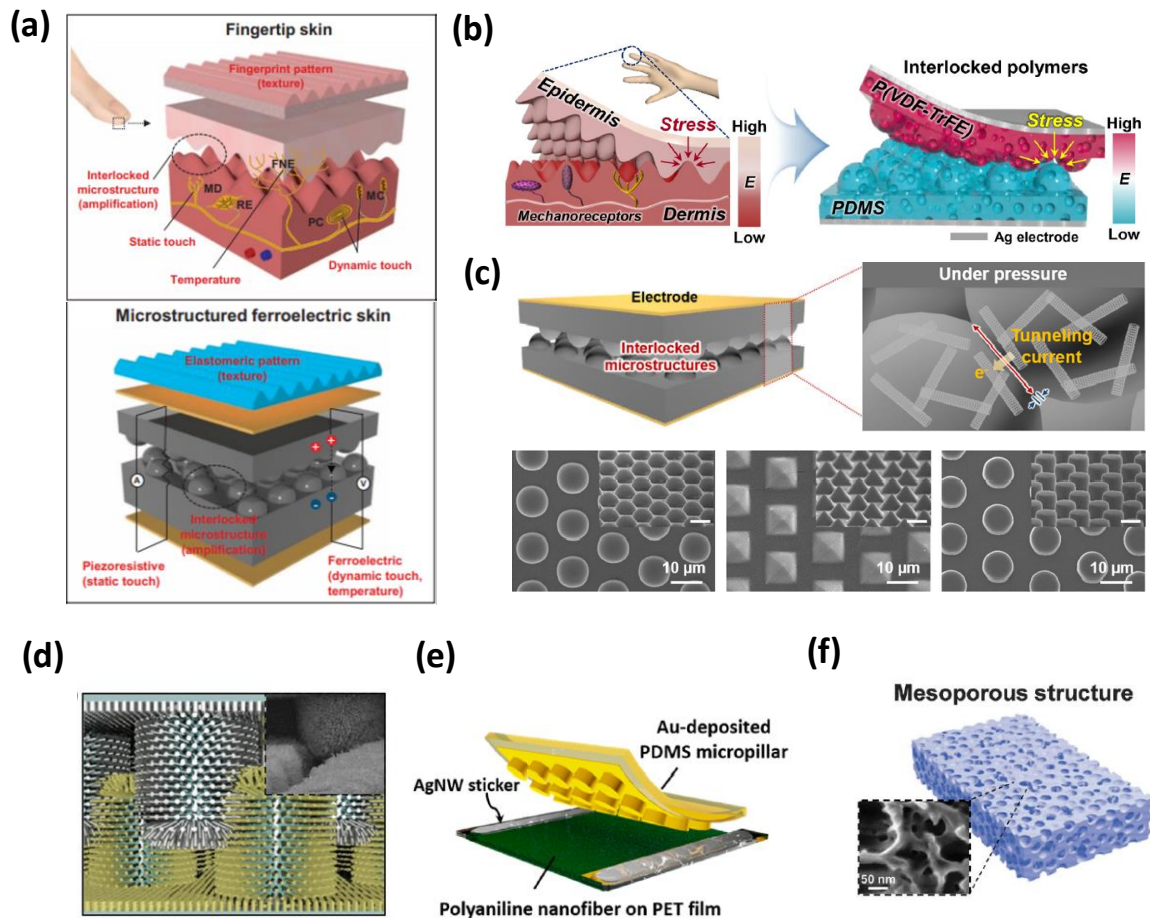


**Figure 1.7.** E-skins employing various microstructure (a) PVDF/rGO micro-dome interlocked structure with sensing capabilities in both piezoresistive and piezoelectric modes.<sup>17</sup> (Park et al. *Science advances*, **2015**, *1*, e1500661.) (b) Porous triboelectric sensor with P(VDF-TrFE) as the upper active layer and PDMS as bottom active layer.<sup>83</sup> (Ha et al. *ACS nano*, **2018**, *12*, 3964-3974.) (c) CNT/PDMS interlocked pressure sensor with micro-dome, micro-pyramid and micro-pillar.<sup>38</sup> (Park et al. *NPG Asia Materials*, **2018**, *10*, 163) (d) hierarchical structure with ZnO nanowire on the micro-pillar structure.<sup>84</sup>(Ha et al. *Advanced Functional Materials*, **2015**, *25*, 3203-3209.) (e) Au deposited micro-pillar structure facing with polyaniline/PET film.<sup>85</sup>(Park et al. *ACS nano*, **2015**, *9*, 9974-9985.) (f) Mesoporous PVDF-film-based piezoelectric nanogenerators.<sup>86</sup>(Mao et al. *Advanced Energy Materials*, **2014**, *4*, 1301624.)

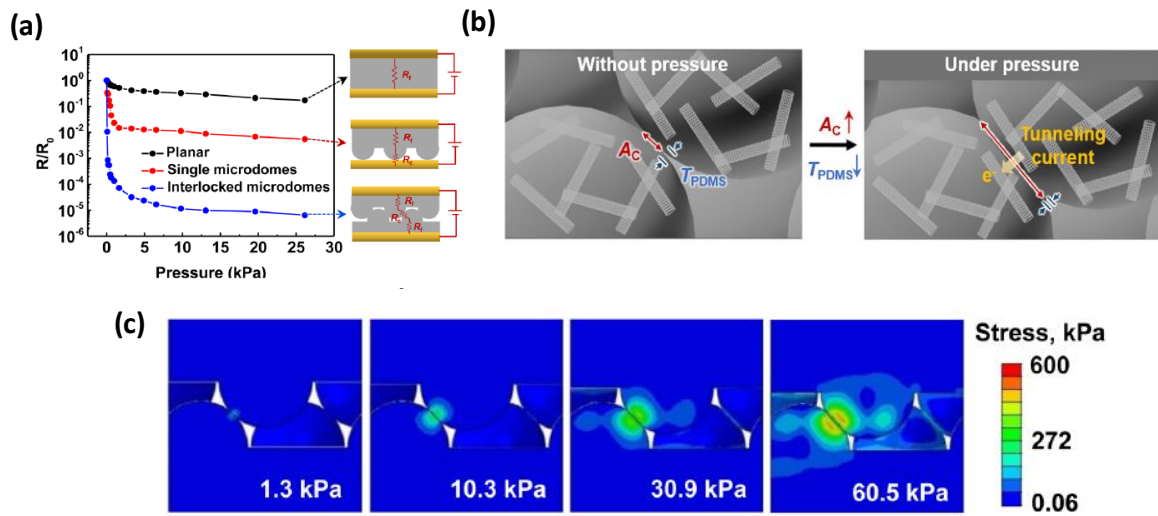


**Figure 1.8.** The structural effect of micro-structure in terms of electrical tunneling effect and local stress concentration. (a) The different sensing profile of planar, single micro-dome and interlocked micro-dome.<sup>7</sup> (Park et al. *ACS nano*, **2014**, 8, 4689-4697.) (b) Scheme of the electrical tunneling effect when the surface of micro-dome contacts (c) Fine element analysis of the interlocked micro-dome structure as the applied pressure.<sup>38</sup> (Park et al. *NPG Asia Materials*, **2018**, 10, 163)

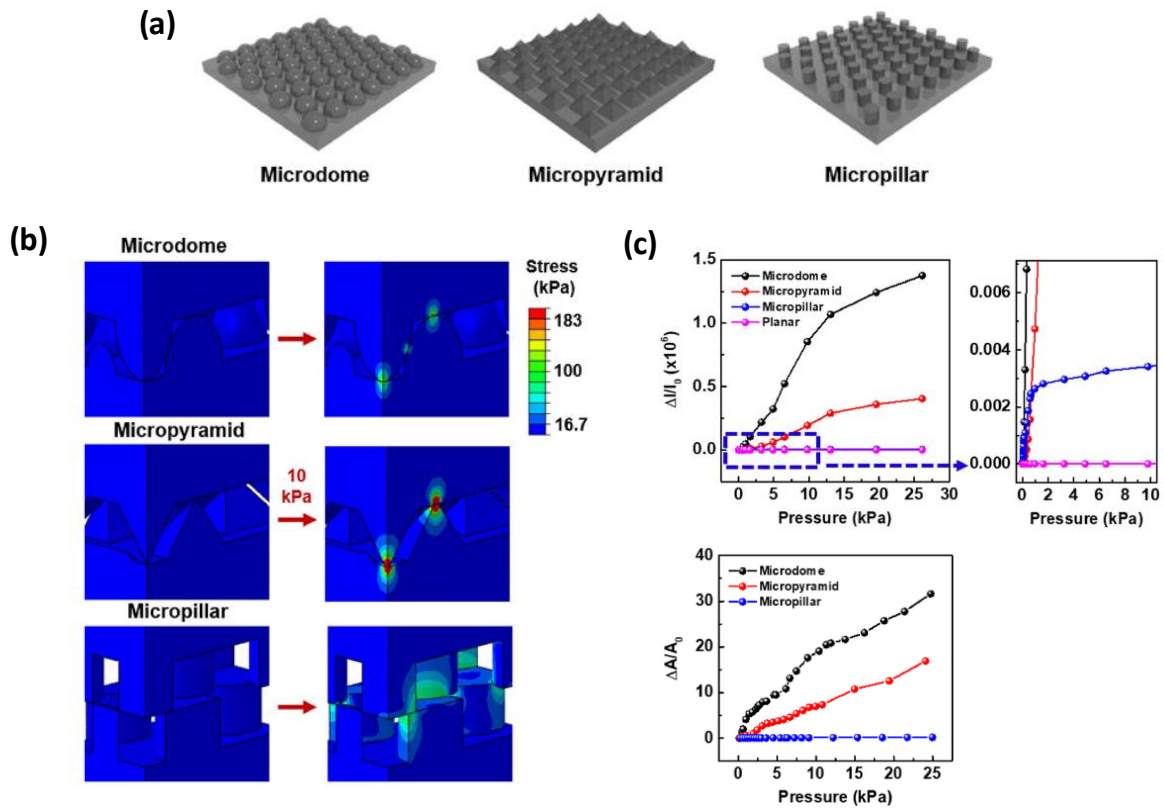


**Figure 1.9.** Comparison of structural effect in interlocked micro-structure (a) The scheme of fabricated micro-structure including micro-dome, micro-pyramid and micro-pillar. (b) Fine element analysis of interlocked micro-dome, micro-pyramid and micro-pillar when pressure is applied. (c) different electrical performance of micro-dome, micro-pyramid and micro-pillar in terms of change of the current and the contact area.<sup>38</sup> (Park et al. *NPG Asia Materials*, **2018**. 10. 163)

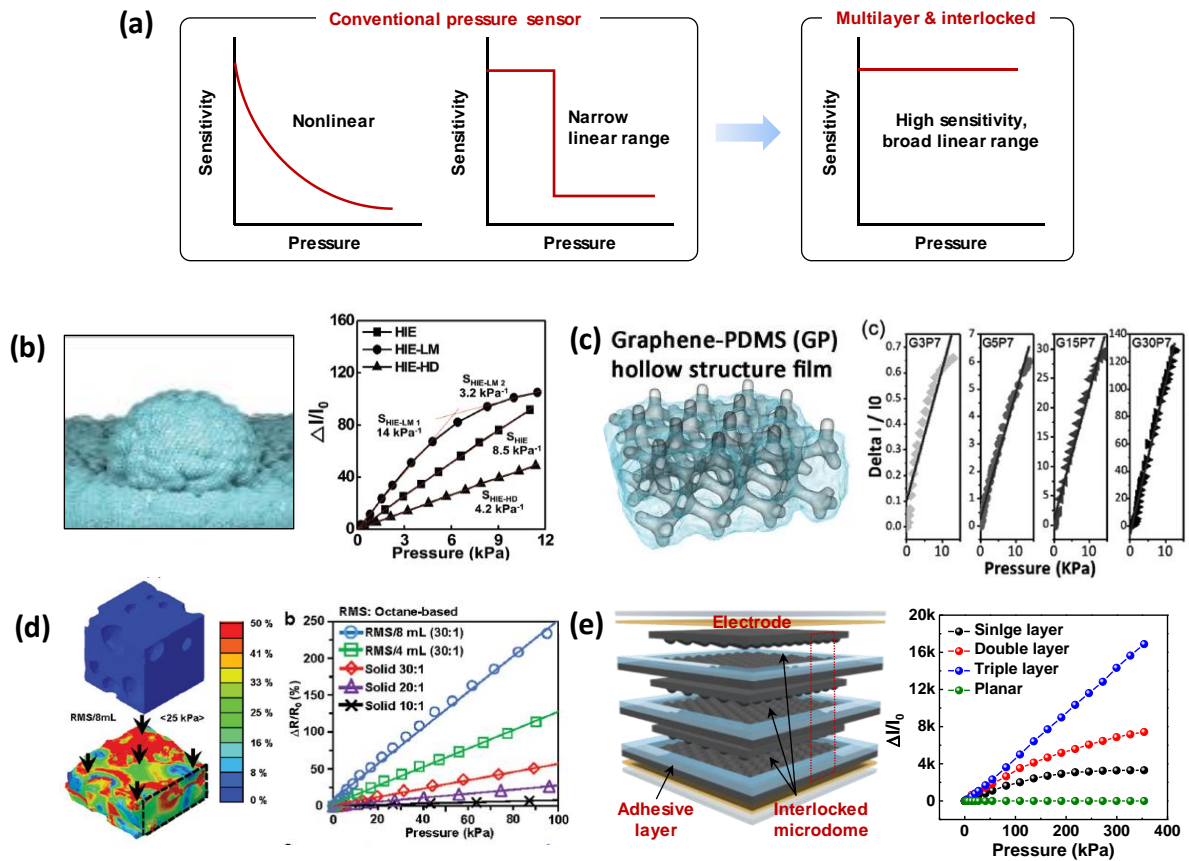


**Figure 1.10.** The endeavor to overcome the limitation of conventional pressure sensor. (a) Scheme showing the 2 different pressure sensing trends conventional pressure sensor and advanced pressure sensor.<sup>53</sup>(Lee et al. *ACS nano*, **2018**. *12*. 4045-4054.) (b) graphene coated hierarchical structure fabricated by chemical vapor deposition (CVD) method.<sup>54</sup>(Bae et al. *Advanced Materials*, **2016**. *28*. 5300-5306.) (c) Graphene hollow structure of Ni foam and encapsulation by PDMS.<sup>55</sup>(Luo et al. *Advanced Materials*, **2017**. *29*. 1702675.) (d) Porous structure of MWCNTs and PDMS using reverse micelles.<sup>1</sup>(Jung et al. *Advanced Materials*, **2014**. *26*. 4825-4830.) (e) Multilayered structure of PVDF/rGO interlocked sensor.<sup>53</sup>(Lee et al. *ACS nano*, **2018**. *12*. 4045-4054.)

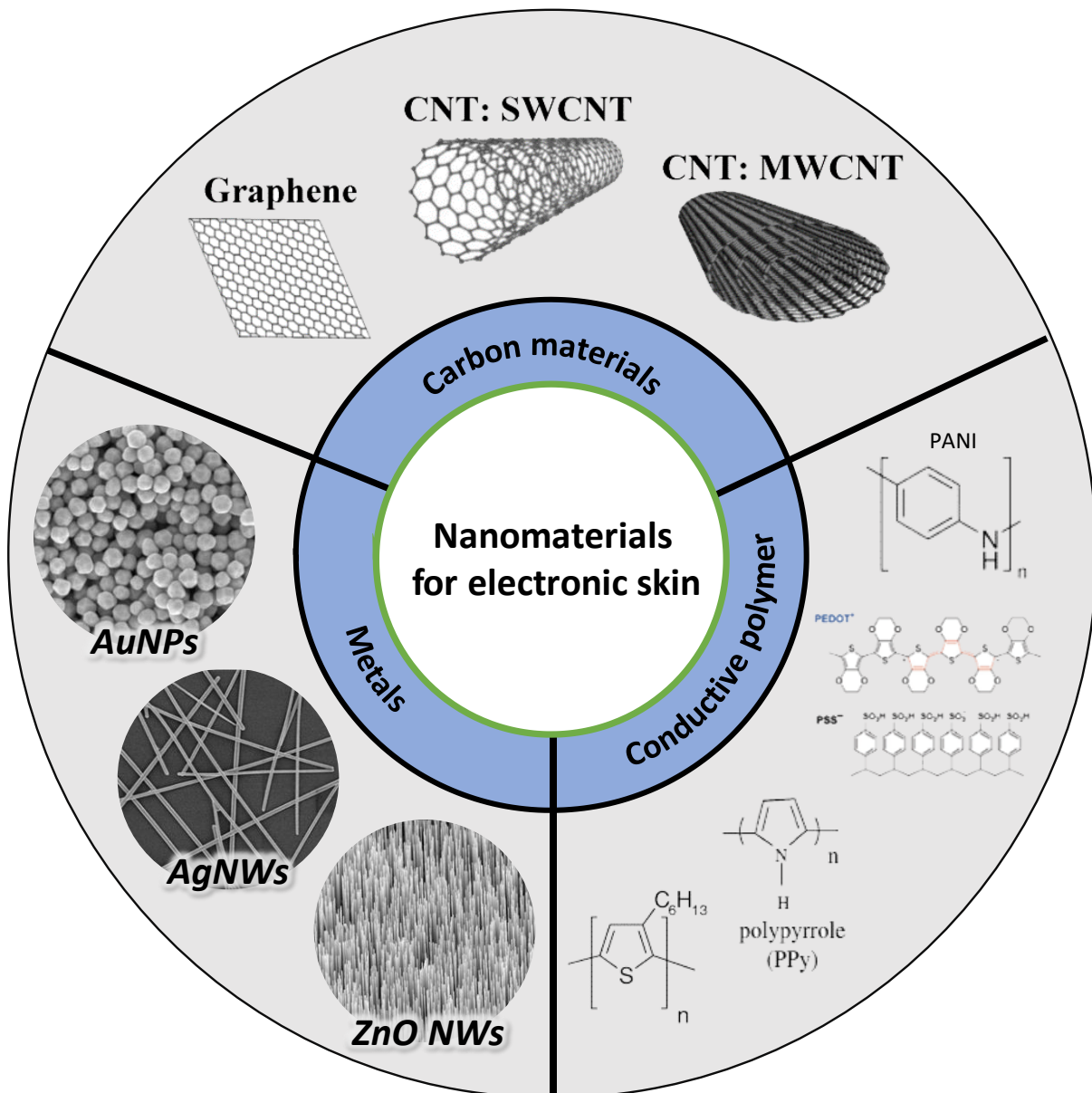


**Figure 1.11.** The conductive nanomaterials widely used in the fabrication of e-skins. In clockwise, carbon nanomaterials including graphene, CNTs and conductive polymers including PEDOT:PSS, polyaniline (PANI), polypyrrole (Ppy) and P3HT are demonstrated. Lastly, metals including gold nanoparticles (AuNPs), silver nanowires (AgNWs), ZnO nanowires are illustrated.

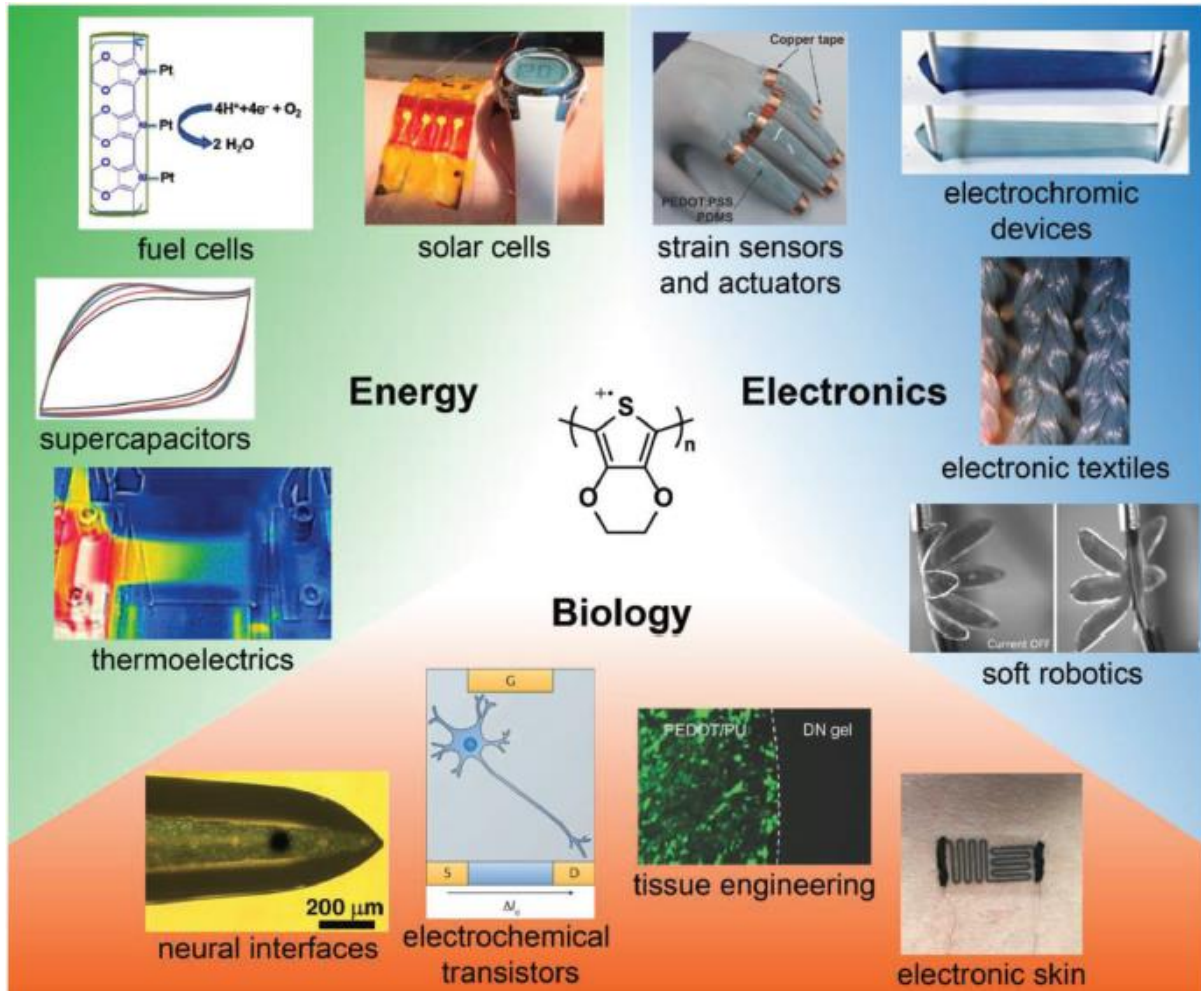


**Figure 1.12.** The application field of stretchable and conductive PEDOT in energy, electronics, and biology: thermoelectrics, supercapacitors, fuel cells, solar cells, strain sensors and actuators, electrochromic devices, electronic textiles, soft robotics, electronic skin, tissue engineering, organic electrochemical transistors (OECTs), and neural interfaces.<sup>65</sup>(Kayser et al. *Advanced Materials*, **2019**, 31, 1806133.)



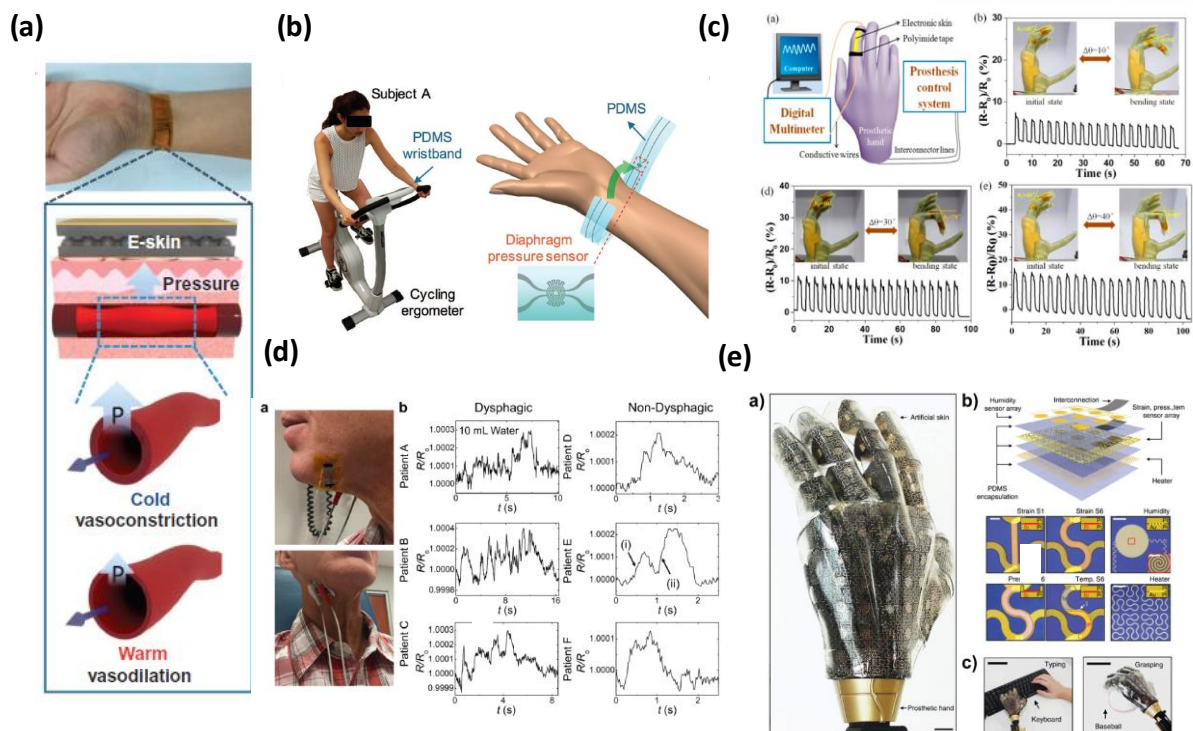
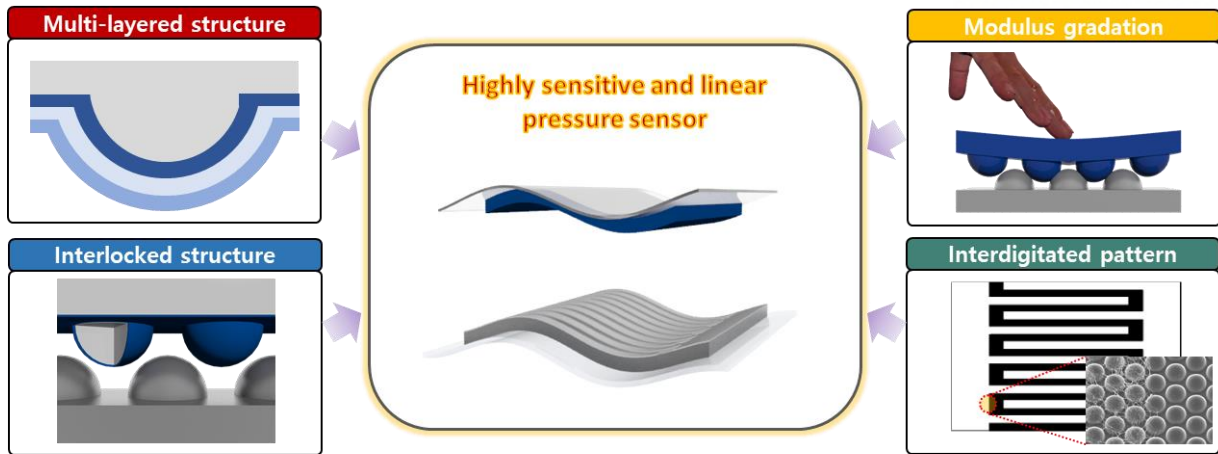


**Figure 1.13.** Application of electronic skin in wearable devices by detection pressure of the human body. (a) Photograph of e-skin attached on the wrist and schematic of blood pressure when cold and warm.<sup>17</sup> (Park et al. *Science advances*, **2015**. *1*. e1500661.) (b) Wearable devices attached on the wrist and can detects the physiological signal of exercising volunteer.<sup>87</sup> ( Gao et al. *Advanced Materials*, **2017**. *29*. 1701985.) (c) Prosthesis integrated with temperature, humidity and multiple forms of strain sensor.<sup>10</sup>(Hu et al. *ACS applied materials & interfaces*, **2018**. *10*. 38493-38505.) (d) Diagnosis of dysphagic by detection of subtle vibration of the neck.<sup>74</sup>(Ramírez et al. *ACS nano*, **2018**. *12*. 5913-5922.) (e) Pressure sensing device attached on the forehead and detecting cerebral oximetry.<sup>2</sup>(Kim et al. *Nature communications*, **2014**. *5*. 5747. 3)



**Discrimination of subtle difference of tactile sensing**

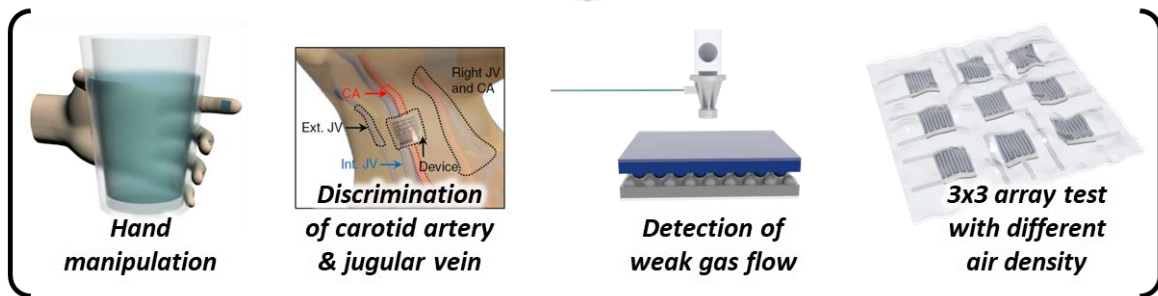


**Figure 1.14.** The main strategies of multi-layered pressure sensor and its application (a) The strategies for enhancement of sensitivity and linearity: Multi-layering, Interlocking, Modulus gradation of up and bottom substrate and interdigitated pattern on electrode (b) Applications of the e-skin for discrimination of subtle difference of tactile and pressure sensing: pressure in hand manipulation, discrimination of carotid artery and internal jugular vein, the detection of weak gas flow and test the spatial distribution and different air density with 3x3 pixel array.

## Experiment

### 2.1 Conductivity control of PEDOT:PSS

As one of the conductive materials, PEDOT:PSS has widely used in sensors or electrode due to their several advantages of easy solution processability, fine formation of film, high conductivity and stability. The pristine PEDOT has poor solubility in water, which can be improved by the doped material of PSS. Because the PSS is insulator, which forms the shell encircles around the conductive PEDOT grain, it has a relatively high resistance to be used for the pressure sensor. The disorder of the PEDOT:PSS grain, without connection of each grain of PEDOT, can be rearranged by various methods including addition of polar additives or surfactant and post treatment with polar solvent.<sup>88</sup> The added solvent can wash away the insulator PSS part to the side and arrange the PEDOT core grain to be connected to each other with an increase in conductivity (**Figure 2.1a**).

In the fabrication of multi-layered pressure sensor, ethylene glycol (EG, Sigma Aldrich) was added to PEDOT:PSS (CLEVIOS PH1000) as the conductivity enhancer, which is biocompatible and easy solution processible. Addition to the EG, to increase the wettability and make fine film on the PDMS substrate, surfactants including 4-Dodecylbenzenosulfonic acid (Sigma Aldrich) and 3-methacryloxypropyltrimethoxysilane (Sigma Aldrich) was added and stirred for 6 hours (**Figure 2.1b**). Varying the amount of EG, we set 170  $\Omega$  as the lowest resistance of solution in this condition, when ethylene glycol is added to 1:20 in PEDOT:PSS. Subsequently, Polyurethane dispersion (PUD) (Alberdingk U3251) was added in PEDOT:PSS solution and stirred at room temperature for 1 h.

## 2.2 Fabrication of substrates with interlocked structures

In **figure 2.2**. The fabrication process of interlocked sensor with multi-layering and interdigitated electrode is demonstrated. The sensor is interlocked with PEDOT:PSS multi-coated micro-dome patterned PDMS and Pt and AgNWs coated micro-dome patterned TPU under the interdigitated mask. To fabricate the micro-dome patterned active layer, a mixture of PDMS and curing agent with 5 to 1 ratio cast onto the micro-dome patterned silicon mold and dried at 80 °C for 2 h. On the annealed PDMS substrate, prepared PEDOT:PSS solution was coated with multiple spin-coating. The PEDOT:PSS solution was filtered using 0.45 μm PVDF syringe filters and spin coated on the prepared PDMS which was treated with O<sub>2</sub> plasma for 5 min. At first, solution with the highest conductivity was coated and annealed for 10mins at 100 °C. And before coating 2nd layer of PEDOT:PSS solution, 1st layer coated PDMS layer was treated with O<sub>2</sub> plasma moderately for 30 s, to increase the wettability, but not to decompose the conductivity of 1<sup>st</sup> layer. By repeating the above process, the layer of PEDOT:PSS solution is stacked to 3 layer, as the conductivity of each layer decreases (**Figure 2.2a**).

Fabricated PDMS layer is integrated onto the electrode layer of TPU film. The TPU film is also replicated from the micro-dome patterned silicon mold and sputtered with Pt (EMITECH, K575X) under the mask of interdigitated pattern for 3 min. Because of the possibility of crack only with Pt, the AgNWs is spray-coated on the Pt layer by repetition of spraying 3 s and drying 7 s for 2 min. After finishing the spray-coating, TPU layer with Pt and AgNWs is treated with O<sub>2</sub> plasma for 1 min to remove PVP layers and enhance the contact between AgNWs (**Figure 2.2b**). The fabricated sensor has a thickness of 200 μm with high flexibility and mechanical durability.

### 2.3 Characterizations

**Thickness measurement of PEDOT:PSS/PUD film** Because of the thin thickness of the PEDOT:PSS/PUD film by spin-coating method, it is difficult to be distinguished from the PDMS surface in SEM (Cold FE-SEM S-4800) analysis. To obtain a clear image of the cross section of the film on the microdome patterned PDMS, Au is deposited on the bare PDMS surface and PEDOT:PSS/PUD film, sandwiching the target film.<sup>40</sup> In **Figure 2.3a**, the overall thickness of multi-layered PEDOT:PSS/PUD film can be measured between the 60~70 nm of Au thin film. The film thickness at the microdome's peak is about 65 nm. And valley between 2 different microdomes is covered by PEDOT:PSS/PUD film with a thickness of 321 nm. In addition, to distinguish the thickness of PEDOT:PSS/PUD film with different conductivity, Au is deposited between 1<sup>st</sup> and 2<sup>nd</sup> layer with a thickness of 100 nm. The film thickness is approximately 85 and 30 nm at microdome's peak and 187 and 85nm at valley between 2 different microdomes.

**The multi-layered PEDOT:PSS on the micro-patterned PDMS** The conductivity of the PEDOT:PSS/PUD composite controlled by the addition of EG and other surfactants can have various values of the sheet resistance depending on the amounts of them. In **figure 2.4a**, varied sheet resistance of the PEDOT:PSS/PUD composite was verified by 4-probe method (4200-SCS, Keithley). Thin PEDOT:PSS film and PEDOT:PSS/PUD film was coated on the Si-wafer to evaluate the difference of resistance depending on the EG. As demonstrated in **figure 2.4a**, the sheet resistance of PEDOT:PSS film decreases as the amount of EG increase, with saturation point at 1:20 ratio of addition of EG. In this point, the sheet resistance of PEDOT:PSS film is 170  $\Omega$  and it increases to 225  $\Omega$  with addition of 50 wt% of PUD. By means of elastic property of PUD, the addition of PUD helps the PEDOT:PSS/PUD composite endure the high pressure until 100 kPa. Beyond that point, the sheet resistance of PEDOT:PSS film slightly increases, which reaches to 225  $\Omega$  when added.

**SEM analysis of interdigitated electrode** The surface of interdigitated patterned electrode with Pt and AgNWs was analyzed by SEM image (**Figure 2.4b**). AgNWs are well coated and connected on Pt sputtered micro-dome TPU. To verify the stability of the electrode, SEM analysis was conducted again after applied pressure with 100 kPa for 300 times. The cracks on the surface are hardly observed and AgNWs are well connected, compared to the PDMS electrode showing many cracks and disconnected AgNWs on the surface.

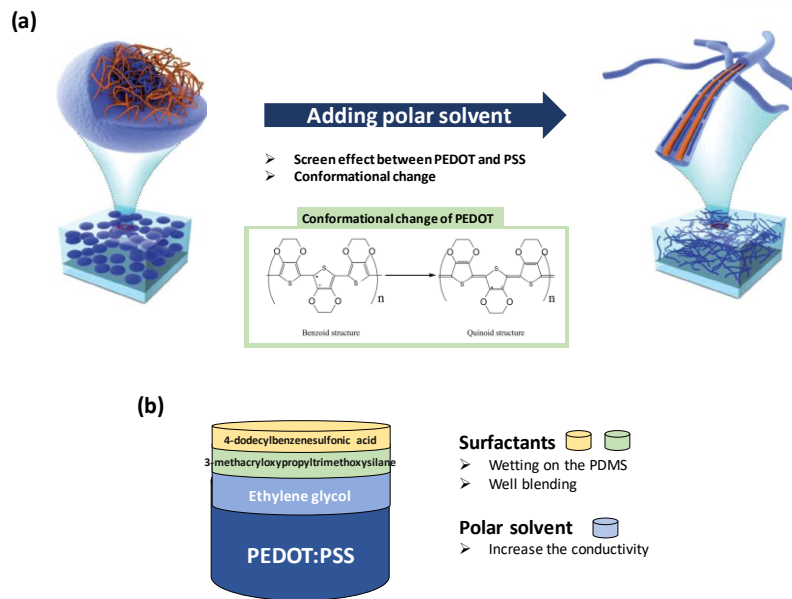


**Figure 2.1.** Recipe of the PEDOT:PSS solution and sheet resistance characterization (a) Schematic illustration of the arrangement of PEDOT and PSS grain by addition polar solvent.<sup>89</sup> (Kim et al. *Advanced Materials*, **2014**, 26, 2268–2272) (b) Recipe of the PEDOT:PSS solution for better wettability and blending

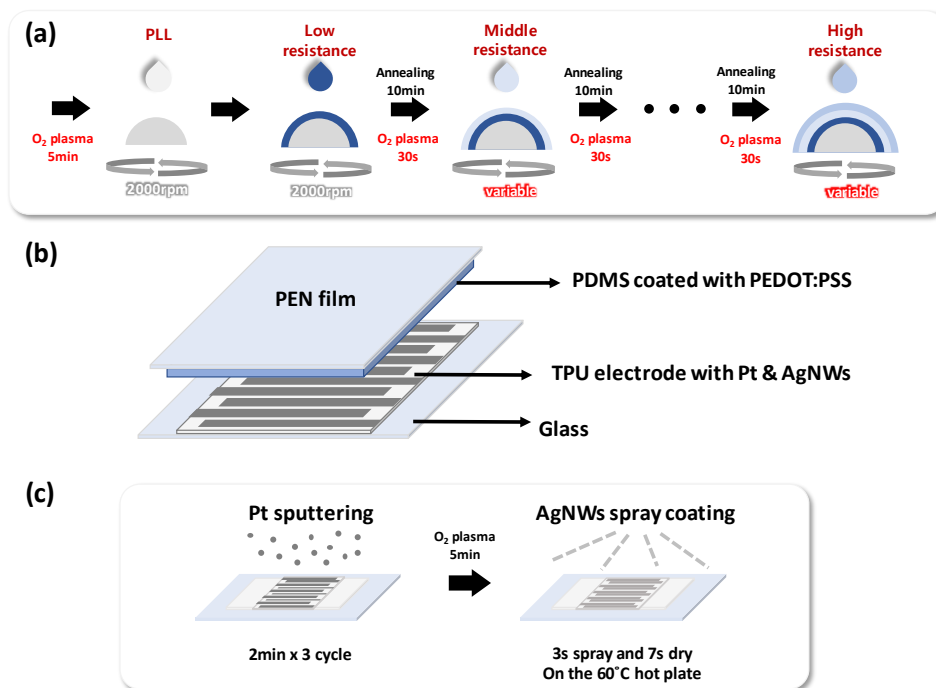


**Figure 2.2.** Fabrication procedure of multi-layering e-skins (a) Sequential coating of PLL and PEDOT:PSS/PUD solution with different conductivity (b) Scheme of the interlocked e-skins. (c) Fabrication of the electrode with Pt sputtering and AgNWs spray coating.

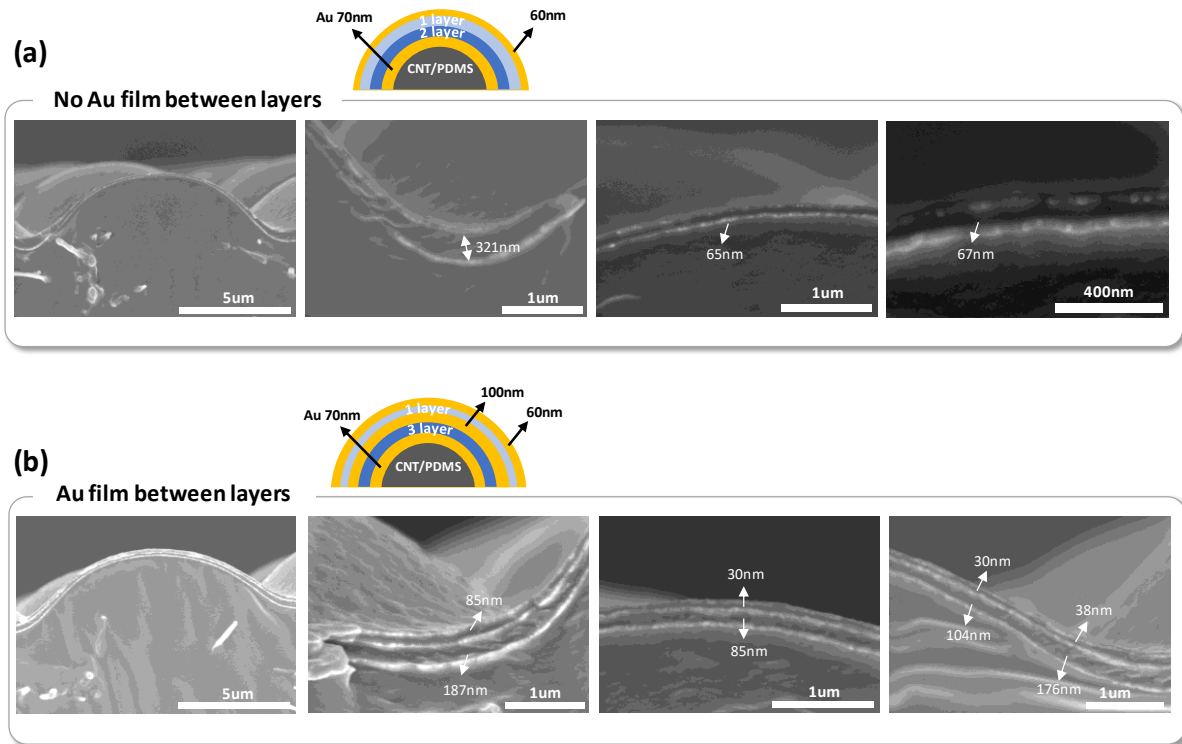
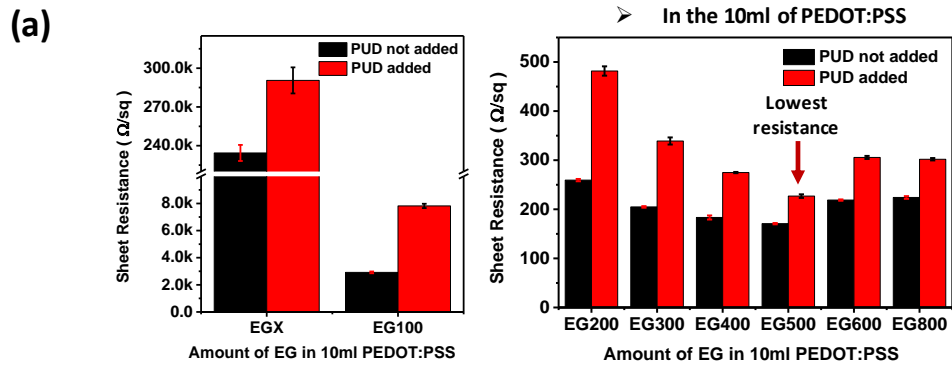


**Figure 2.3.** SEM image of the thickness of PEDOT:PSS/PUD film coated on the microdome patterned matrix (a) Au thin film(60nm) that was sandwiched between the PEDOT:PSS/PUD film (55nm of 3 layer) on the microdome patterned CNT/PDMS matrix to distinguish the PEDOT:PSS film. (b) Au film inserted between the PEDOT:PSS/PUD film with different conductivity to discriminate each film of the PEDOT:PSS.



(b)

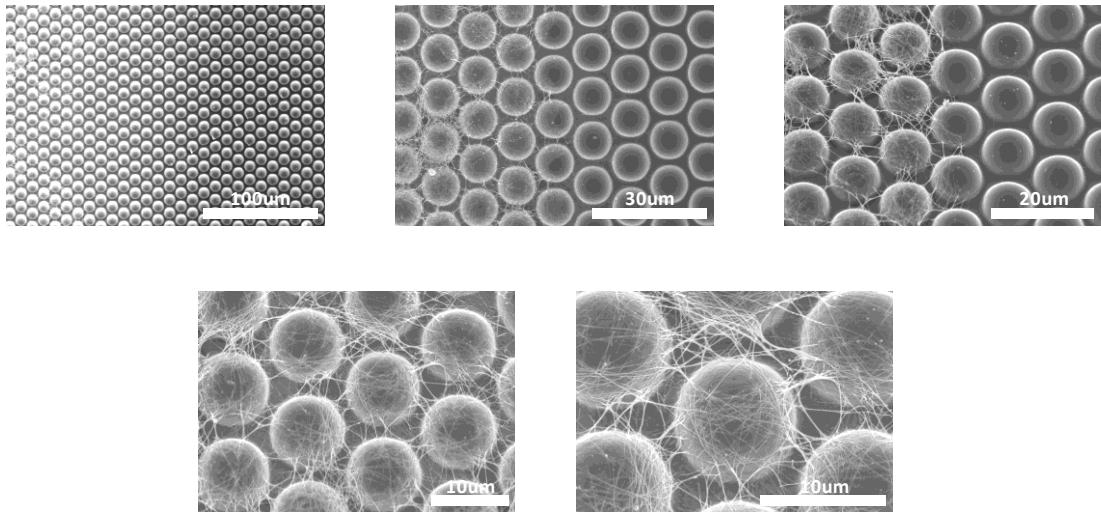


**Figure 2.4.** (a) The sheet resistance of PEDOT:PSS and PEDOT:PSS/PUD thin film depending on the added ethylene glycol. (b) SEM image of Pt sputtered and AgNWs spray-coated microdome TPU with different magnification.



## Results and Discussion

### 3.1 Sensing performance of multi-layered sensors

**Figure 3.1a** shows the schematic illustration of the multi-layering effect on the highly dynamic resistance variation. PEDOT:PSS/PUD with different conductivity is multi-layered on the micro-dome patterned PDMS substrates, which facilitate 7 order of large resistance change from the range of  $10^9 \Omega$  to  $10^2 \Omega$ . Dynamic change of resistance entails the enhancement of sensitivity which is defined as  $S = (\Delta I/I_0)/\Delta P$ , where  $I$  is the current of the pressure sensor and  $P$  is the applied pressure. The multi-layered PEDOT:PSS/PUD films with elastic property experience step-by-step compression under the applied pressure, which enables easy control of initial, middle and saturation resistance (**Figure 3.1c**). To demonstrate the effect of multi-layered PEDOT:PSS/PUD composites with interlocked micro-structures on the pressure sensitivity, we compared the electrical performance by applying pressure depending on the number of layers.

In **Figure 3.2c**, single layered PEDOT:PSS/PUD pressure sensor with thickness of 45 nm shows lower sensitivity confirmed compared to 2 and 3 layered sensors. It is because that the single layered sensor has low initial resistance of  $2.3 \times 10^7 \Omega$ , which causes narrow resistance variation. Moreover, the low resistance of single layered sensor exhibits drastic decrease of sensitivity from  $89600 \text{ kPa}^{-1}$  to  $2000 \text{ kPa}^{-1}$  in the initial pressure range of 5 kPa. Even though it has a very low saturation resistance approximately  $116 \Omega$ , the severe non-linearity and low initial resistance degrades the sensing capabilities of the sensor.

On the other hand, the linearity and sensitivity of the e-skins is improved by multi-layering of different conductivity of PEDOT:PSS/PUD composites at the 45 nm of thickness in 1<sup>st</sup> layer. As previously mentioned, single coated PEDOT:PSS/PUD composites show a low sensitivity due to the low initial resistance. Therefore, on top of the single-layered PEDOT:PSS film with the lowest sensitivity, the solution with higher resistance than 1<sup>st</sup> layer is stacked as 2<sup>nd</sup> and 3<sup>rd</sup> layer with 60 k $\Omega$  and 300 k $\Omega$ , respectively. Because the initial contact resistance is determined by the resistance of the outermost layer, the increase of resistance of the outer layer leads to increase of initial resistance. Therefore, the addition of 2<sup>nd</sup> and 3<sup>rd</sup> layer gradually increases the initial resistance, resulting in the improvement of the sensitivity of the sensors. In addition, the added layer mitigates the rapid saturation and alleviates the rapid decrease of sensitivity in the low pressure region. The 2<sup>nd</sup> and 3<sup>rd</sup> layer with higher resistance act as a buffer, which increases the linearity of the detection. As illustrated in **Figure 3.2c**, the sensitivity of the sensor increases as the number of layer increases, which is led by the increase of resistance of the outermost layer. Furthermore, **Figure 3.2d**

demonstrates the sensitivity and assures the improvement of detection linearity as the number of layers increase. As a result, by multi-layering of PEDOT:PSS/PUD composites with different conductivity, high sensitivity and linearity was achieved simultaneously.

### 3.2 Effect of conductivity and thickness of layers

Depending on the thickness and conductivity of the layer, the resistance change in response to the applied pressure can be adjusted. 1<sup>st</sup> layer has the greatest effect on controlling the overall sensitivity, because it critically affects the saturation resistance. The sensing behavior depending on the thickness of the 1<sup>st</sup> layer is shown in **Figure 3.3**. Here, the thickness of 1<sup>st</sup> layer was controlled from 30 nm to 85 nm in one layered sensors by the number of spin-coating. When the first layer thickness is 30 nm, the conductive pathway cannot be formed due to the thin thickness, resulting in the high initial resistance of  $7 \times 10^9 \Omega$ . This high resistance results in the high sensitivity in the low pressure regime, which saturates quickly. By increasing the thickness, the initial resistance gradually decreases down to  $2 \times 10^7 \Omega$  and  $8 \times 10^5 \Omega$  for thickness of 45 nm and 85 nm, respectively. This decreased resistance leads to the narrow variation of resistance and current in response to the applied pressure, resulting in the decreased sensitivity.

The thickness effect on 2 layered sensors is shown in **Figure 3.4a-b**. Because of the 2<sup>nd</sup> layer with the higher resistance of 60 k $\Omega$  compared to the 1<sup>st</sup> layer, the initial resistance of 2 layered sensors increases to the range of  $1 \times 10^9 \Omega$ . The increased initial resistance leads to the enhanced resistance variation, which highly affects the overall sensitivity. In addition, the sensitivity is affected by the saturation resistance, which is determined by the thickness of the 1<sup>st</sup> layer. As the thickness of the 1<sup>st</sup> layer increases, the saturation resistance decreases and the sensitivity of the sensor increases, as confirmed in figure **3.4b**

**Figure 3.4d-f** display the variation of resistance, current, and sensitivity of 3 layered e-skins. The increase of thickness of 1<sup>st</sup> layer deteriorates the linear pressure detection, which causes the rapid decrease of resistance. As the thickness of 1<sup>st</sup> layer increases, the thickness of 2<sup>nd</sup> and 3<sup>rd</sup> layer is relatively negligible, inducing non-linear pressure detection similar with single layered sensors. Accordingly, the R square value of the linear plot decreases from 0.99 to 0.98 and 0.96 for the thickness of 30 nm, 45nm and 85nm of 1<sup>st</sup> layer, respectively. **Figure 3.4f** indicates that the sensitivity rapidly decreases with the increase of pressure as the thickness of 1<sup>st</sup> layer increases. Therefore, we conclude that the thickness of 45nm for 1<sup>st</sup> layer satisfies both high sensitivity and linearity.

To elucidate the multi-layering effect on the sensitivity and conductivity, we compared the sensitivity depending on the conductivity of 2<sup>nd</sup> layer in double layered sensors (**figure 3.5**). The resistance of 1<sup>st</sup> layer was fixed at 225  $\Omega$ , and 2<sup>nd</sup> layer was stacked with the varied resistance of 300 k $\Omega$ , 60 k $\Omega$ , and 8 k $\Omega$ . When the 2<sup>nd</sup> layer is stacked with 300 k $\Omega$ , the high initial resistance

increases the sensitivity in the initial pressure range. However, the large difference of resistance between 1<sup>st</sup> layer and 2<sup>nd</sup> layer leads to the non-linear detection tendency and continuous decrease of sensitivity. As reducing the resistance of 2<sup>nd</sup> layer, the initial resistance decreases, resulting in the decrease of sensitivity. In addition, when the resistance difference between the 1<sup>st</sup> and 2<sup>nd</sup> layer decreases, the overall pressure detection profile follows the trend of single layer, which shows a larger decrease of sensitivity in the low pressure range and the rapid saturation of resistance. These results indicate that the conductivity of layers affects both the sensitivity and linearity of pressure sensors.

### 3.3 Comparison of sensitivity

The most notable feature of multi-layered e-skin is the tunable sensitivity and linearity through the control of the number of layers, conductivity and thickness, which leads to the simultaneous achievement of high sensitivity and linearity. Compared to reported pressure sensing devices so far, the pressure sensor with multilayered PEDOT:PSS/PUD has the highest sensitivity of  $3.1 \times 10^5 \text{ kPa}^{-1}$  with the linear detection over broad pressure sensing range of 100 kPa (**Table 1**). In previous reports, attaining both high sensitivity and linearity was highly challenged due to the trade-off characteristics between them. Most of sensors with the high sensitivity over  $100 \text{ kPa}^{-1}$  either can detect a limited pressure range or show a non-linear sensing profile.<sup>90, 91</sup> As illustrated in **Table 1**, the high sensitivity of the  $9.8 \times 10^4 \text{ kPa}^{-1}$ <sup>42</sup> and  $1907 \text{ kPa}^{-1}$ <sup>41</sup> only maintained for the pressure of 0.2 kPa and 0.1 kPa, respectively. Beyond this point, the sensitivity rapidly decreases. In the other example, the pressure sensor with an excellent linearity over the pressure range of 260 kPa exhibits the poor sensitivity of  $0.0026 \text{ kPa}^{-1}$ .<sup>92</sup>

Recently, a pressure sensor with multi-layered interlocked structures was reported with an excellent sensitivity of  $47.7 \text{ kPa}^{-1}$ , linearity and broad detection range over 353 kPa.<sup>53</sup> The interlocked PVDF/rGO composites concentrate the applied pressure and it can be accumulated at each contact spot of microdome pattern by multi-layering effect. A number of contacts spot localize the applied stress and retain saturation point, which enhances the sensitivity and linearity. The multi-layer structure made the best use of the characteristics of interlocked structure with mechanical approach.

In our research, we improved the sensitivity by introducing a strategy with multi-layering thin film of PEDOT:PSS/PUD composites on the micro-dome patterned substrate with gradient resistance, which further enhances the sensitivity with linear detection over broad pressure range. Compared to the previous research, multi-layered PEDOT:PSS/PUD thin film has specialty in tuning of the resistance under the pressure application. The gradual compression of the multi-layer enables to control the resistance at initial, middle and saturation resistance, which tailors the sensitivity and linearity of the pressure detection.

### 3.4 Structural contribution to multi-layered sensor

E-skins with interlocked structure has a different modulus of upper and bottom layer, with low modulus PDMS as upper active layer and higher modulus TPU as bottom electrode layer (**Figure 3.6a**). To investigate the structural contribution to the electrical performance of multi-layered pressure sensor, we compared the sensing profile of planar and single dome structure with interlocked one in **Figure 3.6b**. The multi-layering condition of the planar is identical with the interlocked one. Because of the multi-layering effect, planar and single dome structure also have high initial resistance of  $7 \times 10^7$  and  $4 \times 10^9 \Omega$ , respectively. In addition, they show similar saturation resistance with interlocked one. Therefore, planar and single dome structures show a relatively high sensitivity of  $5 \times 10^4$  and  $1.1 \times 10^6 \text{ kPa}^{-1}$  in low pressure range ( $\sim 5 \text{ kPa}$ ), respectively. Then, they show a large decrease in sensitivity down to 621 and  $6 \times 10^4 \text{ kPa}^{-1}$  due to the limited range of elastic deformation of planar structure. On the other hand, the interlocked one exhibits highly linear detection profile. In addition, as previously reported, the interlocked micro-dome structure that mimics the dermis and epidermis structure of human skin effectively concentrates the stress on the small contact area. Localized stress induces the large deformation of the elastic micro-structure, entailing the increase of the contact area. Even though the contact area is small compared to planar, huge relative change of contact area enables the highly sensitive detection of pressure.<sup>38, 53</sup>

In order to attain the high sensitivity of the pressure detection, the stability and conductivity of the electrode is as important as the PEDOT:PSS/PUD multi-layered active layer. As we introduce the micro-dome structured TPU as a substrate of electrode coated by metal-based materials, verification of the stability should be conducted. Generally, it is known that PDMS has weak adhesion with metal such as Au, Pt, which inhibits stable detection of pressure and decreases the durability of the sensors.<sup>93</sup> In SEM image of **figure 3.7**, the PDMS coated only with Pt and Pt/AgNWs shows cracks on the surface of the dome and disconnection of AgNWs after the application of 20 kPa pressure with 300 times. However, in case of TPU, not only AgNWs maintain the connection with each other, but cracks were hardly observed even on the Pt-coated micro-dome surface. In addition to a poor adhesion between metal and PDMS, it can be explained by the difference in modulus between TPU and PDMS. The modulus of TPU is approximately 20~30 MPa<sup>94</sup>, which is 5~7 times larger than the PDMS (3.59 MPa)<sup>83</sup>. The deformation of the elastomer with lower modulus is larger when applying pressure. Unlike the elastomer with deformable property, the metal coated on the surface of the elastomer can be easily damaged by their rigid property. As the materials easily deformed by the applied pressure, the cracks and disconnection of

the metal increases, which destabilizes the sensing performance. In addition, the sensitivity of the detection naturally reduced because the damage of the electrode continuously progressed under the repeated pressure application, which interferes the connection between active layer and electrode. It can be confirmed in **Figure 3.6c**, which shows a clear difference in sensing capabilities between PDMS electrode and TPU electrode. The PDMS electrode exhibits rapid saturation in the initial pressure range since the damage progresses during the detection. However, the detection with TPU electrode shows high linearity in both case of PDMS and TPU active layer, which is induced by the stable connection of metals on the surface of TPU.

### 3.5 Durability and reliability of the multi-layered sensors

For the application of attachable, deformable and durable e-skins in wearable devices, the sensors should have reliable sensing performance and durable mechanical properties. The high sensing reliability and durability of multi-layered PEDOT:PSS/PUD pressure sensor can be confirmed in **Figure 3.8** and **3.9**. When applying the pressure from 0.5 kPa to 10 kPa in real time to measure the response and relaxation time, the sensors exhibit the response time of 130 ms and response time of 13 ms (**Figure 3.8a**). Despite the large difference of resistance between the application and release state of pressure, it turns back to the initial resistance very rapidly. It is attributed to the interlocked structure that provides immediate recovery of surface microstructures.<sup>7</sup> In addition, for the application of step-by-step pressure in real time from 0.5 kPa to 100 kPa, multilayered e-skins show a rapid and highly sensitive response to pressure (**Figure 3.8b**). Stable construction of the multi-layered sensor exhibits moderate hysteresis under loading and unloading of 100 kPa pressure. In addition, **Figure 3.9a** shows that reliable linearity of e-skins can be assured even at different voltages from 0.1 V to 5V with identical sensing performance. Furthermore, our pressure sensor can maintain the pressure sensing performance even after 5000 times of cycling test with 20 kPa of pressure.



### 3.6 Applications of pressure sensors

For the proof-of-concept demonstrations, we conducted several experiments using a high linearity and sensitivity of multi-layered pressure sensor. The multi-layered pressure sensor with high sensitivity and linearity can be applied from the subtle pressure range ( $\sim$  few Pa) such as gas blowing to the large pressure range ( $\sim$  100 kPa), which covers the various manipulations of human touch. **Figure 3.8** shows the piezoresistive response under the weak gas flow from 3 L/min to 10 L/min, which can be converted into a pressure of 0.7 Pa, 1.5 Pa, 3.6 Pa and 4.9 Pa corresponding to the linear fit of the measured electrical performance in **figure 3.2c**. The pressure sensor can clearly distinguish the different pressure of gas flow. In **figure 3.11**, to monitor the pulse rate in real time, multi-layered sensor is attached on the neck. Owing to the high sensitivity and linearity of the sensor, it can discriminate the characteristic peaks of artery pulse signals of P1, P2, and P3, which represents incident, tidal and diastolic waves, respectively. Pulse frequency of the volunteer based on the recorded pulse signal is 85 beats/min, which corresponds to the value for healthy adults.<sup>95</sup> Moreover, the characteristic peak of pulse signal provides the health information including radial augmentation index ( $AI_r = P_2/P_1$ ), diastolic augmentation index ( $DAI_r = P_3/P_1$ ) and digital volume pulse time ( $T_{DVP} = t_{p2} - t_{p1}$ ), where  $t_{p1}$  and  $t_{p2}$  are the time of the first ( $P_1$ ) and second peak ( $P_2$ ), respectively. Based on the monitored carotid artery signal, the value of  $AI_r$ ,  $DAI_r$ , and  $T_{DVP}$  are calculated as 0.73, 0.52 and 0.187s, respectively, which shows a good health condition of volunteer in mid-twenties.<sup>96</sup> Moreover, depending on the position of the sensor on the neck, e-skin can detect the pulse rate of venous blood pressure. As described in **figure 3.11c**, the signal from the internal jugular vein is monitored in real time. When bending volunteer's head back at  $45^\circ$  and facing slightly turned to the left, the pulse rate of the internal jugular vein can be monitored by multilayered sensor on the neck.<sup>97</sup> It has 3 characteristic peaks including A (Atrial contraction), C (Tricuspid bulging, Ventricular contraction) and V (Systolic filling of the atrium) and 2 descents; X (Atrial relaxation) and Y (Early ventricular filling), which can be clearly discriminated in the detected signal.<sup>98</sup>

The flexible and durable properties of multi-layered e-skins enable the pressure detection during the human hand's manipulation. In **figure 3.12a**, the smart gloves are fabricated by attaching e-skins on the fingertip. Wearing the gloves, volunteer grasps the cup containing different amount of water, which corresponds to 25 g, 50 g, 100 g, 150 g, 200 g and 250 g of water. When volunteer wearing smart gloves holds and lifts a cup of water, the sensor attached on the fingertip contacts to the surface of the cup. Depending on the weight of the water contained in the cup, the volunteer would apply different pressure to lift the cup. Therefore, as the weight of the water is heavier, the

resistance decreases more, with higher current change. Detected real-time signal from hand manipulation can be confirmed in **figure 3.12b**

Highly sensitive multi-layered pressure sensor is able to detect the magnitude and spatial distribution of external stimuli. The 3 x 3 sensor array was fabricated with PEN substrate at the top and bottom active layer (**figure 3.13a**). Owing to the high sensitivity and linearity, it can distinguish different stress from the weight in medium pressure region (~20 kPa) (**figure 3.13b-c**). Furthermore, when loading the objects with the shape of Korean consonant “diguet”, we can obtain the image of that consonant on the sensor array by sensing the spatial pressure distribution applied by the shape of “diguet” (**figure 3.13d**). To utilize the high sensitivity of the e-skins, we investigated the discrimination of subtle pressure difference of different gas densities (**figure 3.14**). The tested gases include nitrogen and argon, which have a density of 1.25 g/L and 1.78 g/L, respectively. When blowing a gas with a flow rate of 15 L/min on the 3 x 3 pixel sensor arrays from the same distance of 20 mm, the blow of argon gas, which has a higher density than nitrogen gas, induces the larger variation of resistance compared to the nitrogen gas. Even though the density difference of these gases is very small to be measured by the human skin, the artificial e-skins shows excellent discrimination capabilities.

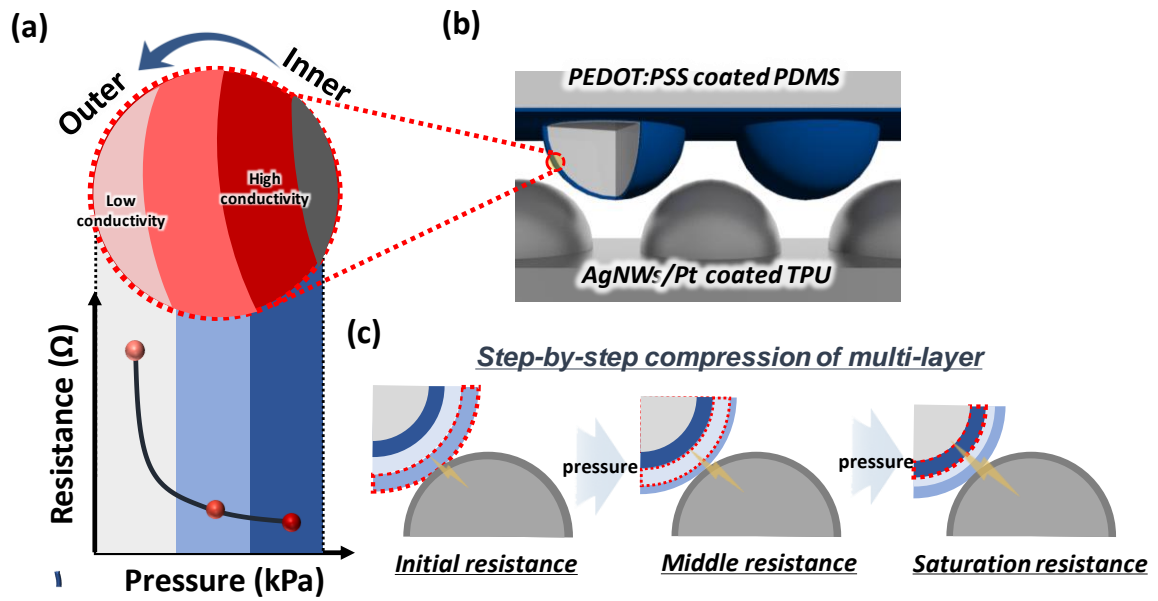


**Figure 3.1.** The Scheme of the multi-layered e-skins interlocked with 2 different layer. (a) Scheme for demonstration of multi-layering effect on resistance change in broad working range. (b) Scheme of the interlocked PEDOT:PSS/PUD coated PDMS and TPU (c) Illustration of step-by-step compression of multi-layered PEDOT:PSS/PUD composite by the applied pressure.

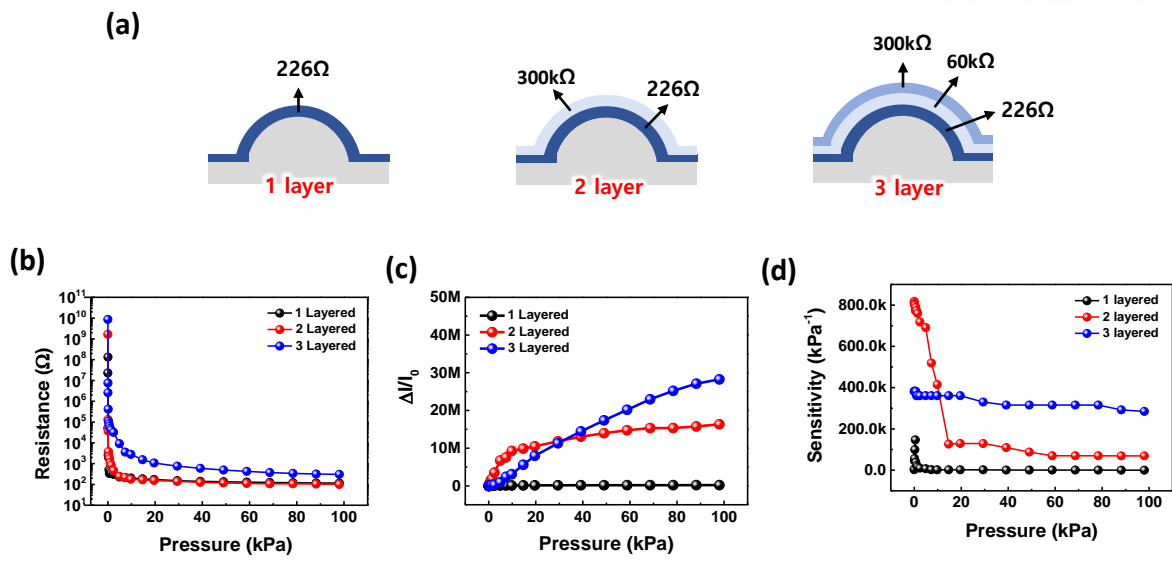


**Figure 3.2.** The sensing performance of multi-layered pressure sensor with a thickness of 45nm of the 1<sup>st</sup> layer. (a) Multi-layering condition with different conductivity in each layer (b-d) The variation of resistance and current and sensitivity depending on the number of layers.

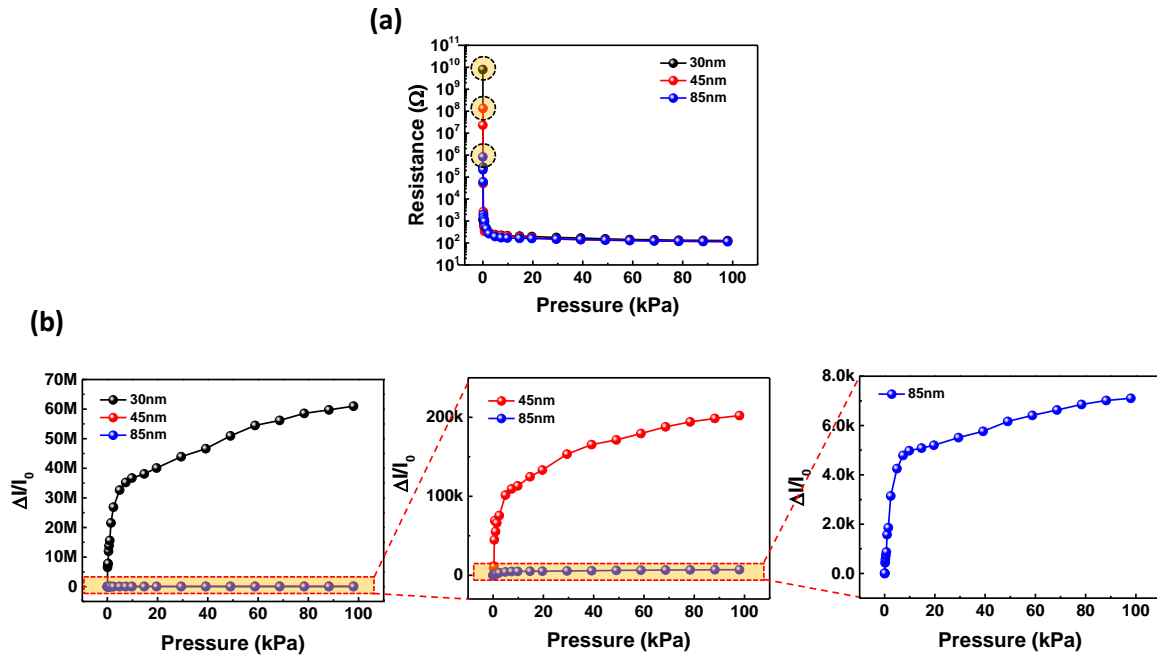


**Figure 3.3.** Thickness effect in 1 layered sensor of PEDOT:PSS/PUD thin film. (a) Variation of resistance depending on the thickness to verify the tendency of initial and saturation resistance. (b) Current variation of 1 layered sensor.

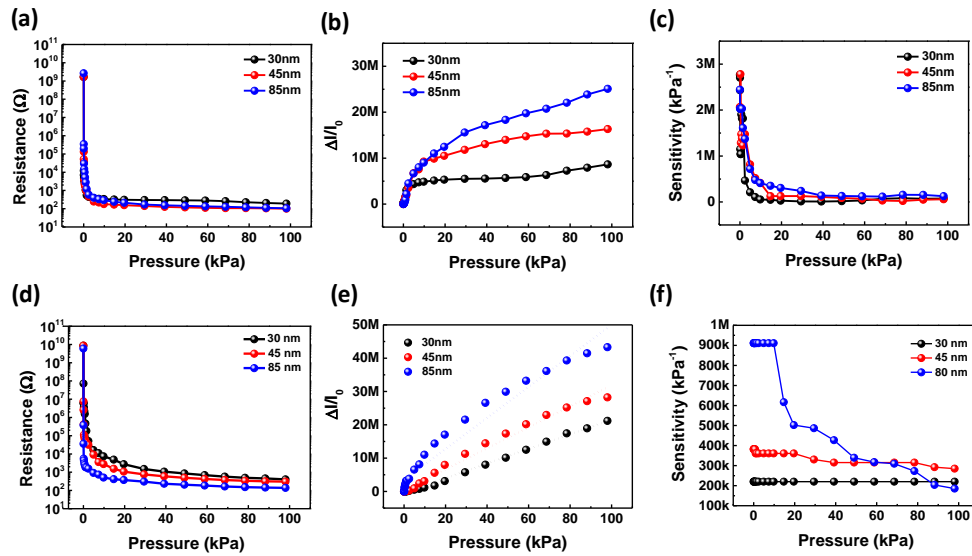


**Figure 3.4.** Effect of thickness on the linearity of multi-layered e-skins (a-c) Sensing performance in resistance and current variation and sensitivity of 2 layered sensor. (d-f) Sensing performance in resistance and current variation and sensitivity of 3 layered sensor.

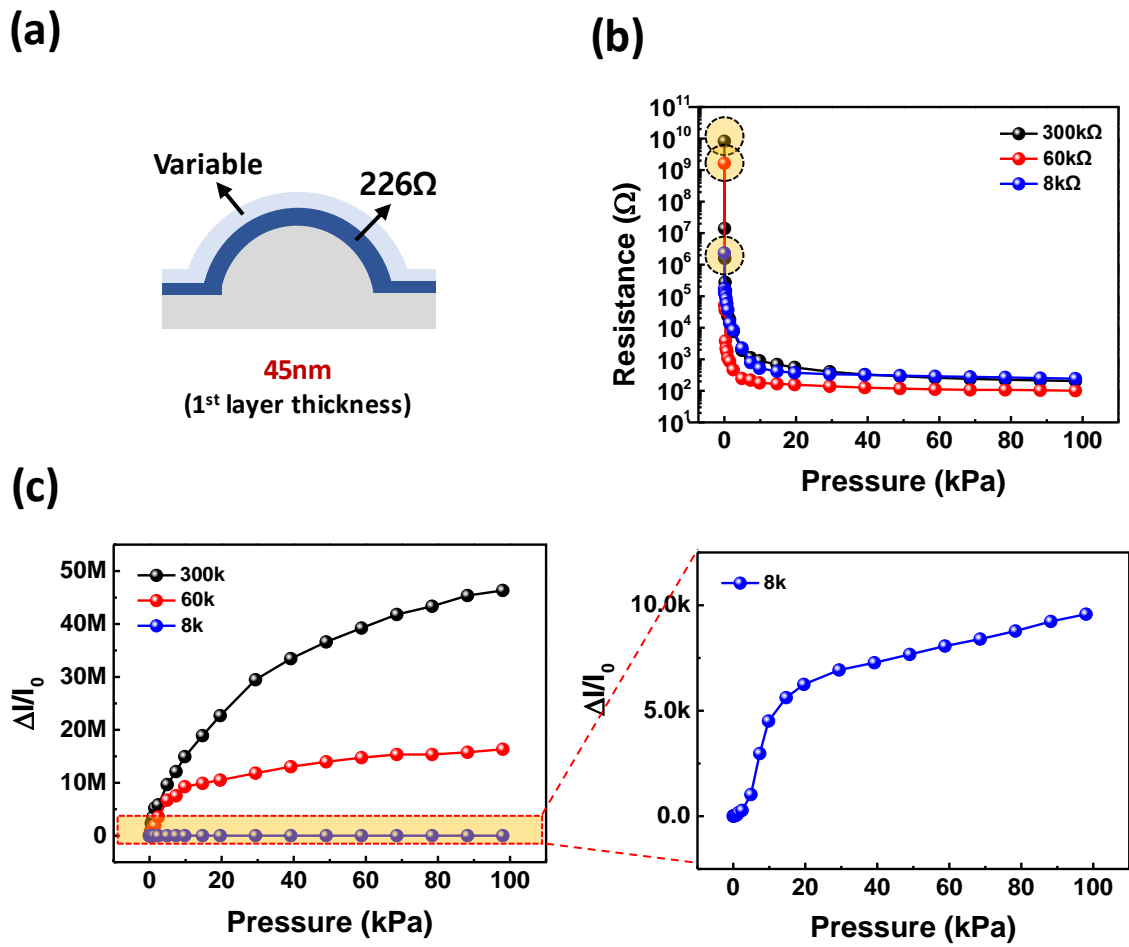


**Figure 3.5.** Sensing performance depending on the conductivity of the 2<sup>nd</sup> layer (a) Layering condition (b) Resistance variation with different conductivity of the 2<sup>nd</sup> layer (c) Current variation.

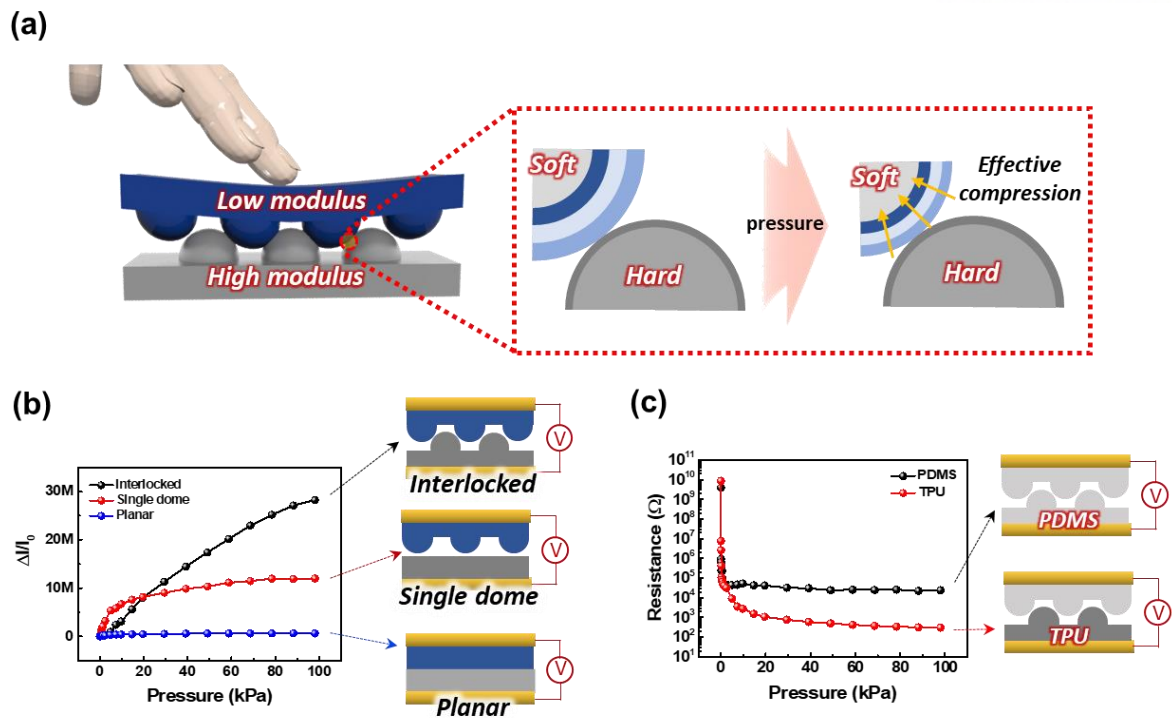


**Figure 3.6.** Structural contribution on the multi-layered pressure sensor. (a) Scheme of interlocked sensor with different modulus of substrate (b) Comparison of sensing performance of different sensor structure with 3 layered sensor and 45nm of the 1<sup>st</sup> layer thickness (c) Different saturation resistance depending on the modulus of upper and bottom substrate.

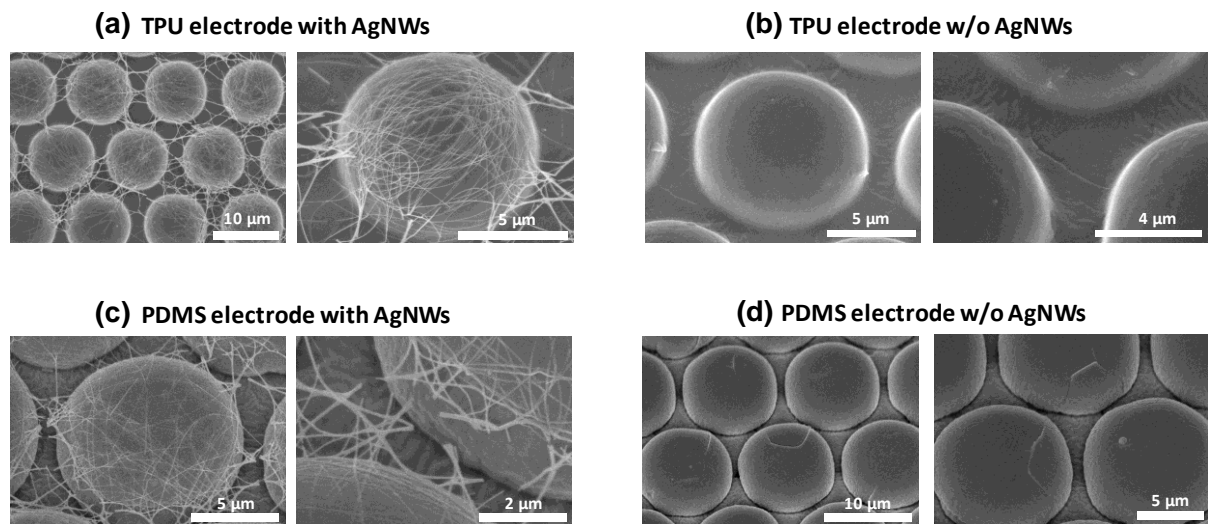


**Figure 3.7.** SEM analysis of microdome patterned electrode. (a) Microdome TPU with Pt and AgNWs. (b) Microdome TPU with Pt (C) Microdome PDMS with Pt and AgNWs. (d) Microdome PDMS with Pt.

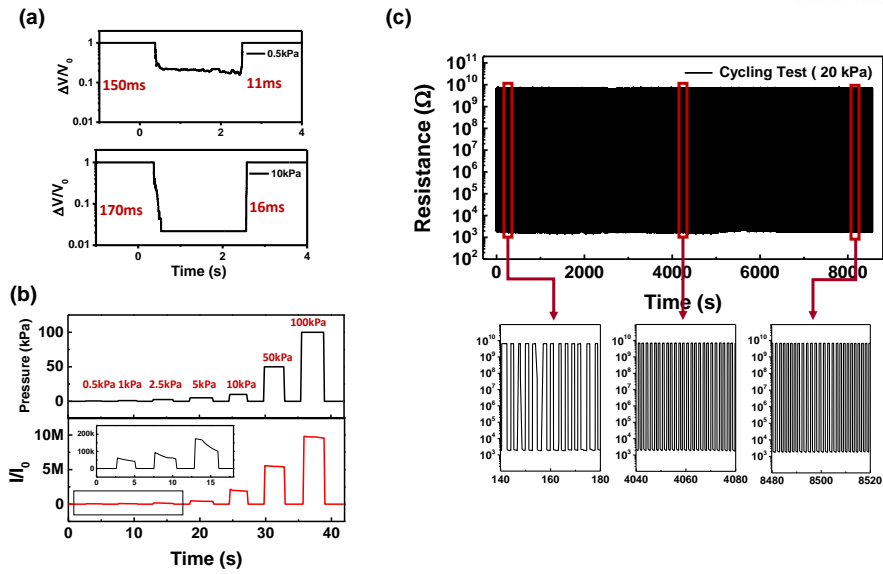


**Figure 3.8.** Reliability and stability test of multi-layered e-skins (a) Cyclic stability test of e-skin under repetitive pressure loading of 20 kPa at a frequency of 0.25 Hz. (b) Real-time monitoring of response and relaxation times for multi-layered e-skins under different pressures of 0.5 kPa and 10 kPa.

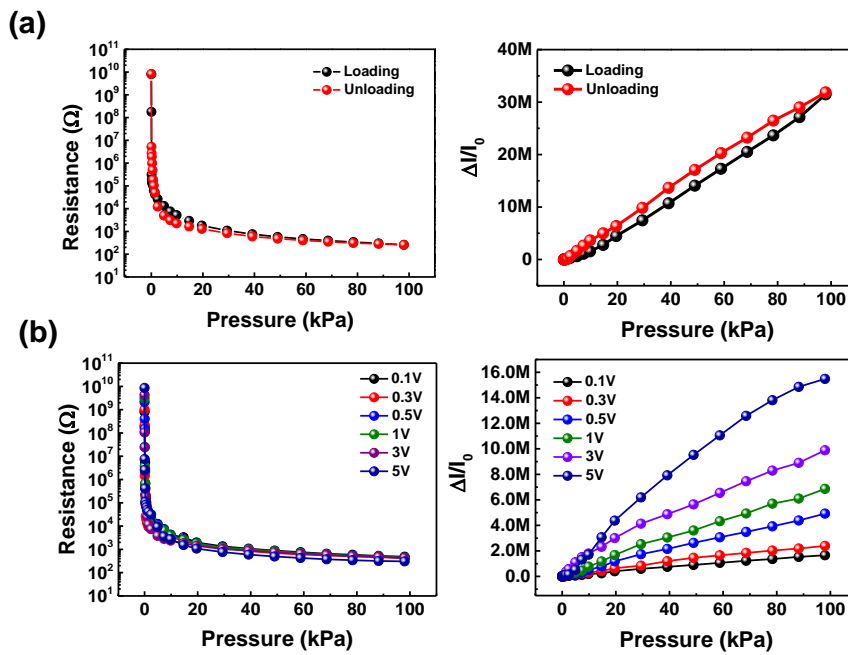


**Figure 3.9.** (a) Hysteresis curve when loading the pressure of 100 kPa and unloading. (b) Sensing performance with resistance and current variation with different applied voltage.



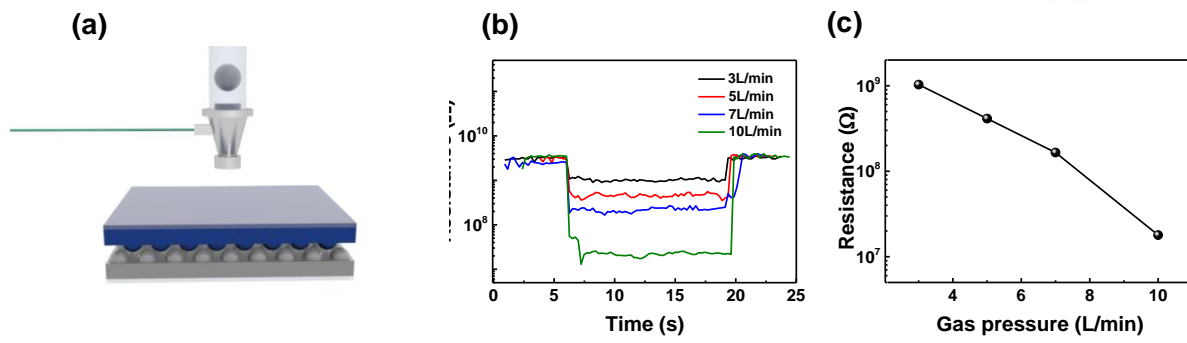


**Figure 3.10.** Application of highly sensitive e-skins into the gas pressure sensing (a) Scheme of weak gas flow on the multi-layered e-skin. (b) Real-time monitoring of resistance variation depending on the flow rate of the gas (c) Resistance change of e-skins as a function of gas flow rate.

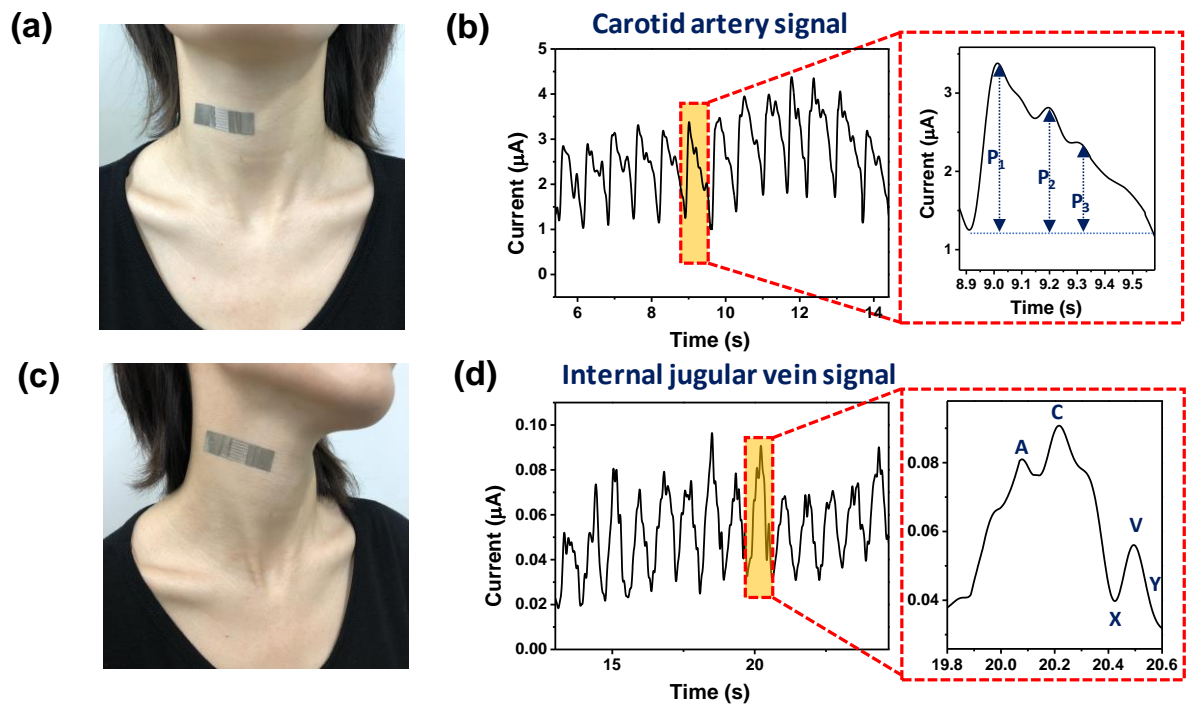


**Figure 3.11.** Application of multi-layered e-skins to health-care monitoring (a) Photograph showing the detection of pulse pressure of carotid artery of the volunteer's neck (b) Monitored real-time pulse signals from carotid artery and characteristic peaks of  $P_1$  (incident wave),  $P_2$  (tidal wave) and  $P_3$  (diastolic wave). (c) Photograph showing detection of pulse pressure of internal jugular vein of volunteer facing slightly turning left. (d) Monitored real-time pulse signals from internal jugular vein and characteristic peaks of A (Atrial contraction), C (Tricuspid bulging, Ventricular contraction) and V (systolic filling of atrium) and 2 descents; X (Atrial relaxation) and Y (Early ventricular filling).

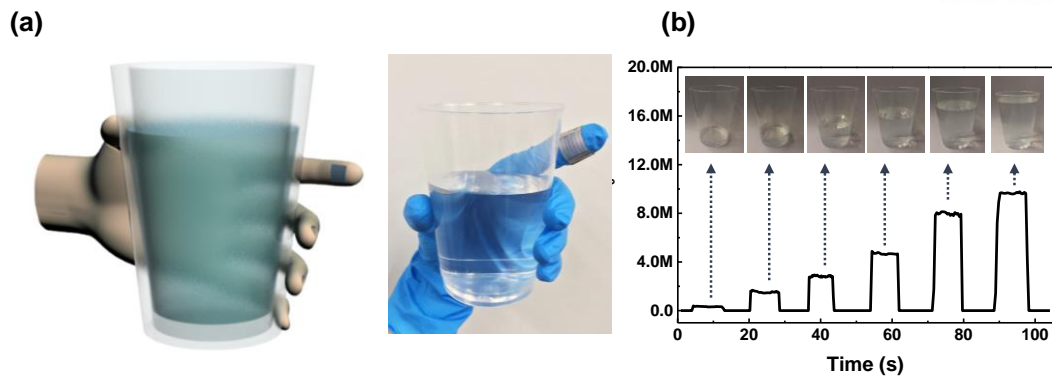


**Figure 3.12.** Application of e-skins into holding cups with different amount of water. (a) Schematic and photograph showing the gloves attached with multi-layered sensor on the fingertip and it is holding cup containing 150g of water. (b) Real-time detection of current variation as the amounts of water increases, which corresponds to 25 g, 50 g, 100 g, 150 g, 200 g and 250 g of water.

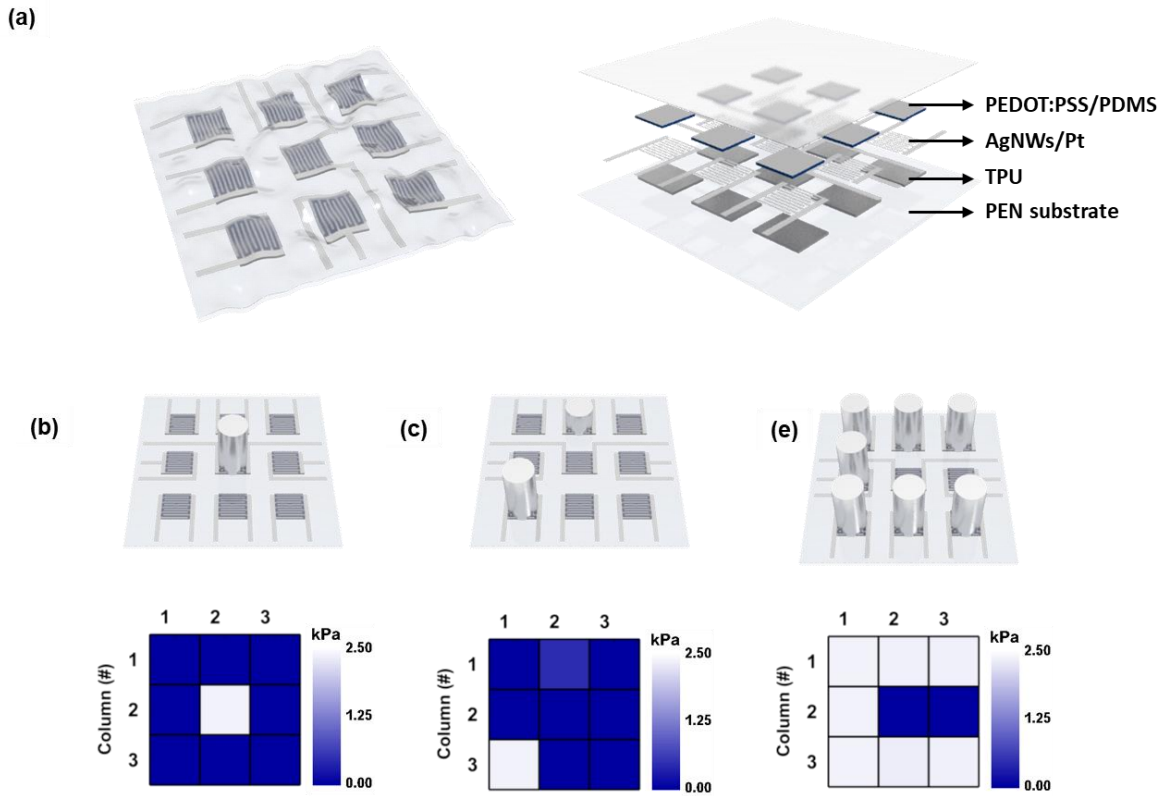


**Figure 3.13.** Scheme of the array and application from low pressure to high pressure. (a) Scheme of fabricated 3x3 array. (b-e) Scheme of the spatial distribution detection with different shapes and weights on the multi-layered 3x3 pixel array

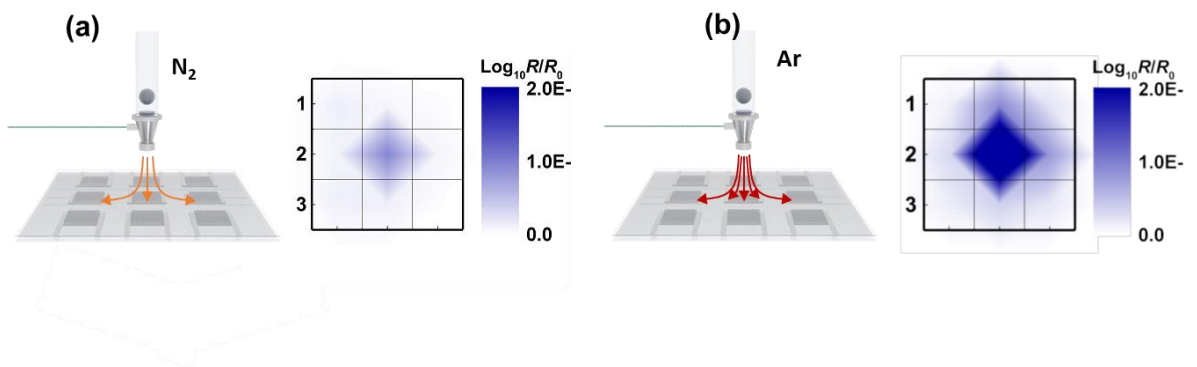


**Figure 3.14.** The scheme illustrating different air density of Ar and N<sub>2</sub> on the multi-layered sensor and detected spatial distribution.

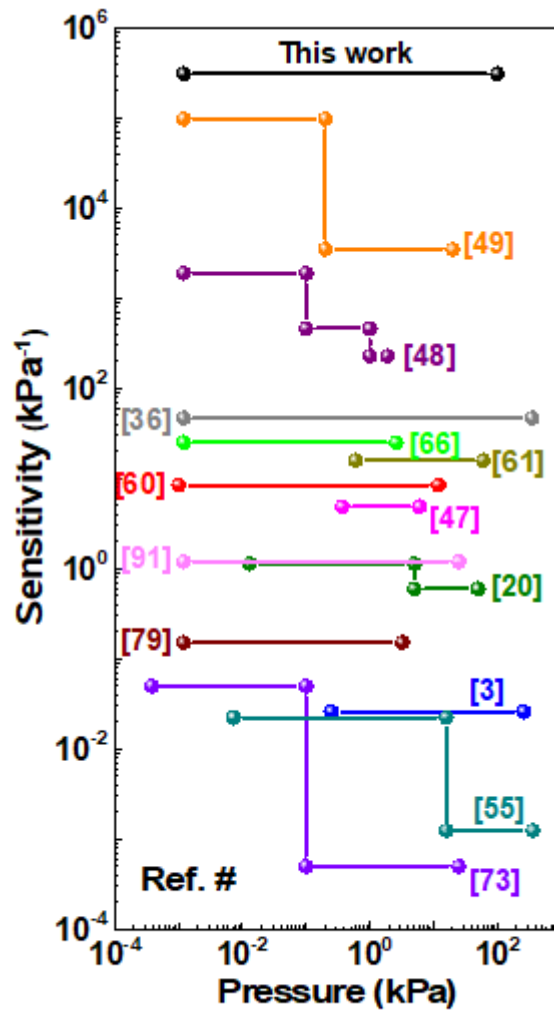


**Table 1.** Linearity table of piezoresistive pressure sensor with characteristics.

## Conclusion

In this research, we demonstrated a highly-sensitive and linearly-responsive flexible pressure sensor, which is achieved by multi-layering of PEDOT:PSS/PUD composites with interlocked structures. The pressure sensor showed the highest sensitivity developed so far with a sensitivity of  $3.1 \times 10^5 \text{kPa}^{-1}$ . Compared to previous pressure sensing devices with low sensitivity or non-linearity, it maintained high sensitivity and linearity in the pressure range of 100 kPa. By introducing multi-layering thin film of PEDOT:PSS/PUD composite, initial resistance and saturation resistance was tuned with the film thickness and conductivity. With the medium thickness of 1<sup>st</sup> layer, the high sensitivity and linearity were simultaneously achieved. In addition, the micro-dome interlocking structure increases the variation of resistance due to the concentration of local stress in the small spot of the dome surface. As a result, the multi-layered sensor exhibits 7 orders change of resistance in the pressure range of  $10^9 \Omega$  to  $10^2 \Omega$ . The pressure sensor shows a rapid response time of 130 ms and relaxation time of 30 ms, with stable and durable sensing performance in real time. Using the high sensitivity of pressure sensor, we demonstrated the proper application fields including the detection of weak gas pressure, pulse rate of human, the pressure when holding a cup of water. Moreover, by fabrication of 3x3 sensor array, our sensor can detect the spatial distribution depending on the weight. Finally, the suggested sensor can discriminate between the different density of gas pressure with 1.25 g/L of nitrogen and 1.78 g/L of argon. Sensing capabilities with high sensitivity and linearity established here can be applicable in various fields such as wearable devices, personalized healthcare monitoring and prosthesis.

## References

1. S. Jung, J. H. Kim, J. Kim, S. Choi, J. Lee, I. Park, T. Hyeon, D. H. Kim, Reverse-micelle-induced porous pressure-sensitive rubber for wearable human-machine interfaces. *Advanced Materials* **2014**, *26*, 4825.
2. J. Kim, M. Lee, H. J. Shim, R. Ghaffari, H. R. Cho, D. Son, Y. H. Jung, M. Soh, C. Choi, S. Jung, Stretchable silicon nanoribbon electronics for skin prosthesis. *Nature communications* **2014**, *5*, 5747.
3. X. Wang, Y. Gu, Z. Xiong, Z. Cui, T. Zhang, Silk-molded flexible, ultrasensitive, and highly stable electronic skin for monitoring human physiological signals. *Adv. Mater.* **2014**, *26*, 1336.
4. Y. Guo, Z. Guo, M. Zhong, P. Wan, W. Zhang, L. Zhang, A Flexible Wearable Pressure Sensor with Bioinspired Microcrack and Interlocking for Full-Range Human-Machine Interfacing. *Small* **2018**, *14*, 1803018.
5. J. Park, Y. Lee, M. Ha, S. Cho, H. Ko, Micro/nanostructured surfaces for self-powered and multifunctional electronic skins. *J. Mater. Chem. B* **2016**, *4*, 2999.
6. M. L. Hammock, A. Chortos, B. C. K. Tee, J. B. H. Tok, Z. Bao, 25th anniversary article: the evolution of electronic skin (e-skin): a brief history, design considerations, and recent progress. *Adv. Mater.* **2013**, *25*, 5997.
7. J. Park, Y. Lee, J. Hong, M. Ha, Y.-D. Jung, H. Lim, S. Y. Kim, H. Ko, Giant tunneling piezoresistance of composite elastomers with interlocked microdome arrays for ultrasensitive and multimodal electronic skins. *ACS nano* **2014**, *8*, 4689.
8. J. Reeder, M. Kaltenbrunner, T. Ware, D. Arreaga-Salas, A. Avendano-Bolivar, T. Yokota, Y. Inoue, M. Sekino, W. Voit, T. Sekitani, Mechanically adaptive organic transistors for implantable electronics. *Advanced Materials* **2014**, *26*, 4967.
9. M. Kaltenbrunner, T. Sekitani, J. Reeder, T. Yokota, K. Kuribara, T. Tokuhara, M. Drack, R. Schwödiauer, I. Graz, S. Bauer-Gogonea, An ultra-lightweight design for imperceptible plastic electronics. *Nature* **2013**, *499*, 458.
10. Y. Hu, X. Liu, L. Tian, T. Zhao, H. Wang, X. Liang, F. Zhou, P. Zhu, G. Li, R. Sun, Multidimensional Ternary Hybrids with Synergistically Enhanced Electrical Performance for Conductive Nanocomposites and Prosthetic Electronic Skin. *ACS applied materials & interfaces* **2018**, *10*, 38493.
11. X. Li, M. Chen, R. Yu, T. Zhang, D. Song, R. Liang, Q. Zhang, S. Cheng, L. Dong, A. Pan, Enhancing Light Emission of ZnO-Nanofilm/Si-Micropillar Heterostructure Arrays by Piezo-Phototronic Effect. *Advanced Materials* **2015**, *27*, 4447.

12. J. H. Koo, S. Jeong, H. J. Shim, D. Son, J. Kim, D. C. Kim, S. Choi, J.-I. Hong, D.-H. Kim, Wearable electrocardiogram monitor using carbon nanotube electronics and color-tunable organic light-emitting diodes. *ACS nano* **2017**, *11*, 10032.
13. D. Rus, M. T. Tolley, Design, fabrication and control of soft robots. *Nature* **2015**, *521*, 467.
14. J. An, T.-S. D. Le, Y. Huang, Z. Zhan, Y. Li, L. Zheng, W. Huang, G. Sun, Y.-J. Kim, All-Graphene-Based Highly Flexible Noncontact Electronic Skin. *ACS applied materials & interfaces* **2017**, *9*, 44593.
15. T. Q. Trung, S. Ramasundaram, B. U. Hwang, N. E. Lee, An all-elastomeric transparent and stretchable temperature sensor for body-attachable wearable electronics. *Adv. Mater.* **2016**, *28*, 502.
16. T. Chen, Q. Shi, M. Zhu, T. He, L. Sun, L. Yang, C. Lee, Triboelectric self-powered wearable flexible patch as 3D motion control interface for robotic manipulator. *ACS nano* **2018**, *12*, 11561.
17. J. Park, M. Kim, Y. Lee, H. S. Lee, H. Ko, Fingertip skin-inspired microstructured ferroelectric skins discriminate static/dynamic pressure and temperature stimuli. *Science advances* **2015**, *1*, e1500661.
18. E. Garcia-Cordero, F. Bellando, J. Zhang, F. Wildhaber, J. Longo, H. Guerin, A. M. Ionescu, Three-Dimensional Integrated Ultra-Low-Volume Passive Microfluidics with Ion-Sensitive Field-Effect Transistors for Multiparameter Wearable Sweat Analyzers. *ACS nano* **2018**, *12*, 12646.
19. J. Yoon, J. Han, B. Choi, Y. Lee, Y. Kim, J. Park, M. Lim, M.-H. Kang, D. H. Kim, D. M. Kim, Three-Dimensional Printed Poly (vinyl alcohol) Substrate with Controlled On-Demand Degradation for Transient Electronics. *ACS nano* **2018**, *12*, 6006.
20. B. C. Tee, C. Wang, R. Allen, Z. Bao, An electrically and mechanically self-healing composite with pressure-and flexion-sensitive properties for electronic skin applications. *Nature nanotechnology* **2012**, *7*, 825.
21. C. M. Boutry, A. Nguyen, Q. O. Lawal, A. Chortos, S. Rondeau-Gagné, Z. Bao, A sensitive and biodegradable pressure sensor array for cardiovascular monitoring. *Advanced Materials* **2015**, *27*, 6954.
22. S. Gong, W. Schwalb, Y. Wang, Y. Chen, Y. Tang, J. Si, B. Shirinzadeh, W. Cheng, A wearable and highly sensitive pressure sensor with ultrathin gold nanowires. *Nature communications* **2014**, *5*, 3132.
23. X. Fu, H. Dong, Y. Zhen, W. Hu, Solution-Processed Large-Area Nanocrystal Arrays of Metal–Organic Frameworks as Wearable, Ultrasensitive, Electronic Skin for Health Monitoring. *Small* **2015**, *11*, 3351.
24. D. Son, J. Lee, S. Qiao, R. Ghaffari, J. Kim, J. E. Lee, C. Song, S. J. Kim, D. J. Lee, S. W. Jun, Multifunctional wearable devices for diagnosis and therapy of movement disorders. *Nature*



*nanotechnology* **2014**, *9*, 397.

25. Y. Huang, X. Fan, S. C. Chen, N. Zhao, Emerging Technologies of Flexible Pressure Sensors: Materials, Modeling, Devices, and Manufacturing. *Advanced Functional Materials* **2019**, *29*, 1808509.
26. H. Tian, Y. Shu, X.-F. Wang, M. A. Mohammad, Z. Bie, Q.-Y. Xie, C. Li, W.-T. Mi, Y. Yang, T.-L. Ren, A graphene-based resistive pressure sensor with record-high sensitivity in a wide pressure range. *Scientific reports* **2015**, *5*, 8603.
27. X. Wang, W.-Z. Song, M.-H. You, J. Zhang, M. Yu, Z. Fan, S. Ramakrishna, Y.-Z. Long, Bionic single-electrode electronic skin unit based on piezoelectric nanogenerator. *ACS nano* **2018**, *12*, 8588.
28. Z. Wu, W. Ding, Y. Dai, K. Dong, C. Wu, L. Zhang, Z. Lin, J. Cheng, Z. L. Wang, Self-Powered Multifunctional Motion Sensor Enabled by Magnetic-Regulated Triboelectric Nanogenerator. *ACS nano* **2018**, *12*, 5726.
29. Y. Lin, J. Chen, M. M. Tavakoli, Y. Gao, Y. Zhu, D. Zhang, M. Kam, Z. He, Z. Fan, Printable Fabrication of a Fully Integrated and Self-Powered Sensor System on Plastic Substrates. *Advanced Materials* **2019**, *31*, 1804285.
30. J. Park, Y. Lee, J. Hong, Y. Lee, M. Ha, Y. Jung, H. Lim, S. Y. Kim, H. Ko, Tactile-direction-sensitive and stretchable electronic skins based on human-skin-inspired interlocked microstructures. *ACS nano* **2014**, *8*, 12020.
31. X. Wang, L. Dong, H. Zhang, R. Yu, C. Pan, Z. L. Wang, Recent progress in electronic skin. *Advanced Science* **2015**, *2*, 1500169.
32. X. Wang, M. Que, M. Chen, X. Han, X. Li, C. Pan, Z. L. Wang, Full Dynamic-Range Pressure Sensor Matrix Based on Optical and Electrical Dual-Mode Sensing. *Advanced Materials* **2017**, *29*, 1605817.
33. F. Yin, J. Yang, H. Peng, W. Yuan, Flexible and highly sensitive artificial electronic skin based on graphene/polyamide interlocking fabric. *Journal of Materials Chemistry C* **2018**, *6*, 6840.
34. C. Yang, L. Li, J. Zhao, J. Wang, J. Xie, Y. Cao, M. Xue, C. Lu, Highly Sensitive Wearable Pressure Sensors Based on Three-Scale Nested Wrinkling Microstructures of Polypyrrole Films. *ACS applied materials & interfaces* **2018**, *10*, 25811.
35. Y. Pang, H. Tian, L. Tao, Y. Li, X. Wang, N. Deng, Y. Yang, T.-L. Ren, Flexible, highly sensitive, and wearable pressure and strain sensors with graphene porous network structure. *ACS applied materials & interfaces* **2016**, *8*, 26458.
36. D. Lee, H. Lee, Y. Jeong, Y. Ahn, G. Nam, Y. Lee, Highly Sensitive, Transparent, and Durable Pressure Sensors Based on Sea-Urchin Shaped Metal Nanoparticles. *Adv. Mater.* **2016**, *28*, 9364.
37. X. Shuai, P. Zhu, W. Zeng, Y. Hu, X. Liang, Y. Zhang, R. Sun, C.-p. Wong, Highly sensitive flexible pressure sensor based on silver nanowires-embedded polydimethylsiloxane electrode with

- microarray structure. *ACS applied materials & interfaces* **2017**, *9*, 26314.
38. J. Park, J. Kim, J. Hong, H. Lee, Y. Lee, S. Cho, S.-W. Kim, J. J. Kim, S. Y. Kim, H. Ko, Tailoring force sensitivity and selectivity by microstructure engineering of multidirectional electronic skins. *NPG Asia Materials* **2018**, *10*, 163.
  39. L. Pan, A. Chortos, G. Yu, Y. Wang, S. Isaacson, R. Allen, Y. Shi, R. Dauskardt, Z. Bao, An ultra-sensitive resistive pressure sensor based on hollow-sphere microstructure induced elasticity in conducting polymer film. *Nature communications* **2014**, *5*, 3002.
  40. C. L. Choong, M. B. Shim, B. S. Lee, S. Jeon, D. S. Ko, T. H. Kang, J. Bae, S. H. Lee, K. E. Byun, J. Im, Highly stretchable resistive pressure sensors using a conductive elastomeric composite on a micropylamid array. *Adv. Mater.* **2014**, *26*, 3451.
  41. H. Li, K. Wu, Z. Xu, Z. Wang, Y. Meng, L. Li, Ultrahigh-Sensitivity Piezoresistive Pressure Sensors for Detection of Tiny Pressure. *ACS applied materials & interfaces* **2018**, *10*, 20826.
  42. J.-H. Pu, X.-J. Zha, L.-S. Tang, L. Bai, R.-Y. Bao, Z.-Y. Liu, M.-B. Yang, W. Yang, Human Skin-Inspired Electronic Sensor Skin with Electromagnetic Interference Shielding for the Sensation and Protection of Wearable Electronics. *ACS applied materials & interfaces* **2018**, *10*, 40880.
  43. D. Kang, P. V. Pikhitsa, Y. W. Choi, C. Lee, S. S. Shin, L. Piao, B. Park, K.-Y. Suh, T.-i. Kim, M. Choi, Ultrasensitive mechanical crack-based sensor inspired by the spider sensory system. *Nature* **2014**, *516*, 222.
  44. K. Takei, Z. Yu, M. Zheng, H. Ota, T. Takahashi, A. Javey, Highly sensitive electronic whiskers based on patterned carbon nanotube and silver nanoparticle composite films. *Proceedings of the National Academy of Sciences* **2014**, *111*, 1703.
  45. S. Jin, Y. Wang, M. Motlag, S. Gao, J. Xu, Q. Nian, W. Wu, G. J. Cheng, Large-Area Direct Laser-Shock Imprinting of a 3D Biomimic Hierarchical Metal Surface for Triboelectric Nanogenerators. *Advanced Materials* **2018**, *30*, 1705840.
  46. C. Pang, G.-Y. Lee, T.-i. Kim, S. M. Kim, H. N. Kim, S.-H. Ahn, K.-Y. Suh, A flexible and highly sensitive strain-gauge sensor using reversible interlocking of nanofibres. *Nature materials* **2012**, *11*, 795.
  47. V. Hayward, A brief overview of the human somatosensory system. In *Musical Haptics*, Springer, Cham: 2018; pp 29.
  48. Q. Hua, J. Sun, H. Liu, R. Bao, R. Yu, J. Zhai, C. Pan, Z. L. Wang, Skin-inspired highly stretchable and conformable matrix networks for multifunctional sensing. *Nature communications* **2018**, *9*, 244.
  49. D. W. Pfaff, N. D. Volkow, *Neuroscience in the 21st century: from basic to clinical*. Springer: 2016.

50. D.-H. Kim, N. Lu, R. Ma, Y.-S. Kim, R.-H. Kim, S. Wang, J. Wu, S. M. Won, H. Tao, A. Islam, Epidermal electronics. *science* **2011**, 333, 838.
51. J. Yuan, Y. Shi, M. Pharr, X. Feng, J. A. Rogers, Y. Huang, A Mechanics Model for Sensors Imperfectly Bonded to the Skin for Determination of the Young's Moduli of Epidermis and Dermis. *Journal of applied mechanics* **2016**, 83, 084501.
52. J. Scheibert, S. Leurent, A. Prevost, G. Debrégeas, The role of fingerprints in the coding of tactile information probed with a biomimetic sensor. *Science* **2009**, 323, 1503.
53. Y. Lee, J. Park, S. Cho, Y.-E. Shin, H. Lee, J. Kim, J. Myoung, S. Cho, S. Kang, C. Baig, Flexible ferroelectric sensors with ultrahigh pressure sensitivity and linear response over exceptionally broad pressure range. *ACS nano* **2018**, 12, 4045.
54. G. Y. Bae, S. W. Pak, D. Kim, G. Lee, D. H. Kim, Y. Chung, K. Cho, Linearly and Highly Pressure-Sensitive Electronic Skin Based on a Bioinspired Hierarchical Structural Array. *Advanced Materials* **2016**, 28, 5300.
55. N. Luo, Y. Huang, J. Liu, S. C. Chen, C. P. Wong, N. Zhao, Hollow-Structured Graphene–Silicone-Composite-Based Piezoresistive Sensors: Decoupled Property Tuning and Bending Reliability. *Advanced Materials* **2017**, 29, 1702675.
56. T. Someya, T. Sekitani, S. Iba, Y. Kato, H. Kawaguchi, T. Sakurai, A large-area, flexible pressure sensor matrix with organic field-effect transistors for artificial skin applications. *Proceedings of the National Academy of Sciences* **2004**, 101, 9966.
57. Y. J. Fan, X. Li, S. Y. Kuang, L. Zhang, Y. H. Chen, L. Liu, K. Zhang, S. W. Ma, F. Liang, T. Wu, Highly Robust, Transparent, and Breathable Epidermal Electrode. *ACS nano* **2018**, 12, 9326.
58. C. Ladd, J. H. So, J. Muth, M. D. Dickey, 3D printing of free standing liquid metal microstructures. *Advanced Materials* **2013**, 25, 5081.
59. S. R. Forrest, M. E. Thompson, Introduction: organic electronics and optoelectronics. *Chemical Reviews* **2007**, 107, 923.
60. D. J. Lee, Y. Oh, J.-M. Hong, Y. W. Park, B.-K. Ju, Light sintering of ultra-smooth and robust silver nanowire networks embedded in poly (vinyl-butylal) for flexible OLED. *Scientific reports* **2018**, 8, 14170.
61. S. Kang, S. Cho, R. Shanker, H. Lee, J. Park, D.-S. Um, Y. Lee, H. Ko, Transparent and conductive nanomembranes with orthogonal silver nanowire arrays for skin-attachable loudspeakers and microphones. *Science advances* **2018**, 4, eaas8772.
62. S. Y. Kim, S. Park, H. W. Park, D. H. Park, Y. Jeong, D. H. Kim, Highly Sensitive and Multimodal All-Carbon Skin Sensors Capable of Simultaneously Detecting Tactile and Biological Stimuli. *Advanced Materials* **2015**, 27, 4178.

63. A. Borenstein, O. Hanna, R. Attias, S. Luski, T. Brousse, D. Aurbach, Carbon-based composite materials for supercapacitor electrodes: a review. *Journal of Materials Chemistry A* **2017**, *5*, 12653.
64. T. A. Skotheim, J. Reynolds, *Handbook of Conducting Polymers, 2 Volume Set*. CRC press: 2007.
65. L. V. Kayser, D. J. Lipomi, Stretchable Conductive Polymers and Composites Based on PEDOT and PEDOT: PSS. *Advanced Materials* **2019**, *31*, 1806133.
66. S. Kim, B. Sanyoto, W. T. Park, S. Kim, S. Mandal, J. C. Lim, Y. Y. Noh, J. H. Kim, Purification of PEDOT: PSS by Ultrafiltration for Highly Conductive Transparent Electrode of All-Printed Organic Devices. *Advanced Materials* **2016**, *28*, 10149.
67. Q. Wei, M. Mukaida, Y. Naitoh, T. Ishida, Morphological change and mobility enhancement in PEDOT: PSS by adding co-solvents. *Advanced materials* **2013**, *25*, 2831.
68. R. Jalili, J. M. Razal, P. C. Innis, G. G. Wallace, One-step wet-spinning process of poly (3, 4-ethylenedioxythiophene): poly (styrenesulfonate) fibers and the origin of higher electrical conductivity. *Advanced Functional Materials* **2011**, *21*, 3363.
69. E. Roh, B.-U. Hwang, D. Kim, B.-Y. Kim, N.-E. Lee, Stretchable, transparent, ultrasensitive, and patchable strain sensor for human-machine interfaces comprising a nanohybrid of carbon nanotubes and conductive elastomers. *ACS nano* **2015**, *9*, 6252.
70. M. K. Choi, O. K. Park, C. Choi, S. Qiao, R. Ghaffari, J. Kim, D. J. Lee, M. Kim, W. Hyun, S. J. Kim, Cephalopod-Inspired Miniaturized Suction Cups for Smart Medical Skin. *Advanced healthcare materials* **2016**, *5*, 80.
71. Y. Park, J. Shim, S. Jeong, G. R. Yi, H. Chae, J. W. Bae, S. O. Kim, C. Pang, Microtopography-guided conductive patterns of liquid-driven graphene nanoplatelet networks for stretchable and skin-conformal sensor array. *Advanced Materials* **2017**, *29*, 1606453.
72. J.-H. Kim, S.-R. Kim, H.-J. Kil, Y.-C. Kim, J.-W. Park, Highly conformable, transparent electrodes for epidermal electronics. *Nano Letters* **2018**, *18*, 4531.
73. K.-I. Jang, S. Y. Han, S. Xu, K. E. Mathewson, Y. Zhang, J.-W. Jeong, G.-T. Kim, R. C. Webb, J. W. Lee, T. J. Dawidczyk, Rugged and breathable forms of stretchable electronics with adherent composite substrates for transcutaneous monitoring. *Nature communications* **2014**, *5*, 4779.
74. J. Ramírez, D. Rodriguez, F. Qiao, J. Warchall, J. Rye, E. Aklile, A. S.-C. Chiang, B. C. Marin, P. P. Mercier, C. Cheng, Metallic Nanoislands on Graphene for Monitoring Swallowing Activity in Head and Neck Cancer Patients. *ACS nano* **2018**, *12*, 5913.
75. M. Bariya, Z. Shahpar, H. Park, J. Sun, Y. Jung, W. Gao, H. Y. Y. Nyein, T. S. Liaw, L.-C. Tai, Q. P. Ngo, Roll-to-Roll Gravure Printed Electrochemical Sensors for Wearable and Medical Devices. *Acs Nano* **2018**, *12*, 6978.

76. J. Y. Oh, Z. Bao, Second Skin Enabled by Advanced Electronics. *Advanced Science* **2019**, 1900186.
77. T. Yokota, P. Zalar, M. Kaltenbrunner, H. Jinno, N. Matsuhisa, H. Kitanosako, Y. Tachibana, W. Yukita, M. Koizumi, T. Someya, Ultraflexible organic photonic skin. *Science advances* **2016**, *2*, e1501856.
78. J. Zhao, S. Han, Y. Yang, R. Fu, Y. Ming, C. Lu, H. Liu, H. Gu, W. Chen, Passive and Space-Discriminative Ionic Sensors Based on Durable Nanocomposite Electrodes toward Sign Language Recognition. *ACS nano* **2017**, *11*, 8590.
79. C. Pang, T. i. Kim, W. G. Bae, D. Kang, S. M. Kim, K. Y. Suh, Bioinspired Reversible Interlocker Using Regularly Arrayed High Aspect-Ratio Polymer Fibers. *Adv. Mater.* **2012**, *24*, 475.
80. J. T. Reeder, T. Kang, S. Rains, W. Voit, 3D, Reconfigurable, Multimodal Electronic Whiskers via Directed Air Assembly. *Adv. Mater.* **2018**, *30*, 1706733.
81. H.-H. Chou, A. Nguyen, A. Chortos, J. W. To, C. Lu, J. Mei, T. Kurosawa, W.-G. Bae, J. B.-H. Tok, Z. Bao, A chameleon-inspired stretchable electronic skin with interactive colour changing controlled by tactile sensing. *Nature communications* **2015**, *6*, 8011.
82. S. Harada, W. Honda, T. Arie, S. Akita, K. Takei, Fully printed, highly sensitive multifunctional artificial electronic whisker arrays integrated with strain and temperature sensors. *ACS nano* **2014**, *8*, 3921.
83. M. Ha, S. Lim, S. Cho, Y. Lee, S. Na, C. Baig, H. Ko, Skin-inspired hierarchical polymer architectures with gradient stiffness for spacer-free, ultrathin, and highly sensitive triboelectric sensors. *ACS nano* **2018**, *12*, 3964.
84. M. Ha, S. Lim, J. Park, D. S. Um, Y. Lee, H. Ko, Bioinspired interlocked and hierarchical design of ZnO nanowire arrays for static and dynamic pressure-sensitive electronic skins. *Adv. Funct. Mater.* **2015**, *25*, 2841.
85. H. Park, Y. R. Jeong, J. Yun, S. Y. Hong, S. Jin, S.-J. Lee, G. Zi, J. S. Ha, Stretchable array of highly sensitive pressure sensors consisting of polyaniline nanofibers and Au-coated polydimethylsiloxane micropillars. *ACS nano* **2015**, *9*, 9974.
86. Y. Mao, P. Zhao, G. McConohy, H. Yang, Y. Tong, X. Wang, Sponge-like piezoelectric polymer films for scalable and integratable nanogenerators and self-powered electronic systems. *Advanced Energy Materials* **2014**, *4*, 1301624.
87. Y. Gao, H. Ota, E. W. Schaler, K. Chen, A. Zhao, W. Gao, H. M. Fahad, Y. Leng, A. Zheng, F. Xiong, Wearable microfluidic diaphragm pressure sensor for health and tactile touch monitoring. *Advanced Materials* **2017**, *29*, 1701985.
88. X. Wang, A. K. K. Kyaw, C. Yin, F. Wang, Q. Zhu, T. Tang, P. I. Yee, J. Xu, Enhancement of

thermoelectric performance of PEDOT: PSS films by post-treatment with a superacid. *RSC Advances* **2018**, *8*, 18334.

89. N. Kim, S. Kee, S. H. Lee, B. H. Lee, Y. H. Kahng, Y. R. Jo, B. J. Kim, K. Lee, Highly conductive PEDOT: PSS nanofibrils induced by solution-processed crystallization. *Adv. Mater.* **2014**, *26*, 2268.

90. G. Ge, Y. Cai, Q. Dong, Y. Zhang, J. Shao, W. Huang, X. Dong, A flexible pressure sensor based on rGO/polyaniline wrapped sponge with tunable sensitivity for human motion detection. *Nanoscale* **2018**, *10*, 10033.

91. J. Shi, L. Wang, Z. Dai, L. Zhao, M. Du, H. Li, Y. Fang, Multiscale hierarchical design of a flexible piezoresistive pressure sensor with high sensitivity and wide linearity range. *Small* **2018**, *14*, 1800819.

92. Y. Pang, K. Zhang, Z. Yang, S. Jiang, Z. Ju, Y. Li, X. Wang, D. Wang, M. Jian, Y. Zhang, Epidermis microstructure inspired graphene pressure sensor with random distributed spinosum for high sensitivity and large linearity. *ACS nano* **2018**, *12*, 2346.

93. D. Koh, A. Wang, P. Schneider, B. Bosinski, K. Oh, Introduction of a chemical-free metal PDMS thermal bonding for fabrication of flexible electrode by metal transfer onto PDMS. *Micromachines* **2017**, *8*, 280.

94. C. Zhang, W. W. Tjiu, W. Fan, S. Huang, T. Liu, A novel approach for transferring water-dispersible graphene nanosheets into organic media. *J. Mater. Chem.* **2012**, *22*, 11748.

95. D. H. Spodick, Survey of selected cardiologists for an operational definition of normal sinus heart rate. *The American journal of cardiology* **1993**, *72*, 487.

96. W. W. Nichols, Clinical measurement of arterial stiffness obtained from noninvasive pressure waveforms. *American journal of hypertension* **2005**, *18*, 3S.

97. J. M. S. C. Chiaco, N. I. Parikh, D. J. Fergusson, The jugular venous pressure revisited. *Cleveland Clinic journal of medicine* **2013**, *80*, 638.

98. C. Wang, X. Li, H. Hu, L. Zhang, Z. Huang, M. Lin, Z. Zhang, Z. Yin, B. Huang, H. Gong, Monitoring of the central blood pressure waveform via a conformal ultrasonic device. *Nature biomedical engineering* **2018**, *2*, 687.

